

# The ANTARES Collaboration

## Contributions to ICRC 2017

### Part I: Neutrino astronomy (diffuse fluxes and point sources)

---

#### Contents

<b>1 New Constraints on all flavour Galactic diffuse neutrino emission with the ANTARES telescope</b>	
PoS (ICRC2017) 942	5
<b>2 Search for a diffuse flux of cosmic neutrinos with the ANTARES telescope</b>	
PoS (ICRC2017) 993	13
<b>3 Neutrinos from the Fermi Bubbles with ANTARES</b>	
PoS (ICRC2017) 1001	21
<b>4 Search for signal emission from unresolved point sources with the ANTARES neutrino telescope</b>	
PoS (ICRC2017) 949	29
<b>5 All-flavor Neutrino Point-like Source Search with the ANTARES neutrino telescope</b>	
PoS (ICRC2017) 986	37
<b>6 Search for time correlations between ANTARES neutrino candidates and IceCube High-Energy Starting Events</b>	
PoS (ICRC2017) 987	45

*35th International Cosmic Ray Conference — ICRC2017*  
*10–20 July, 2017, Bexco, Busan, Korea*

## ANTARES Collaboration Author List

A. Albert<sup>1</sup>, M. André<sup>2</sup>, M. Anghinolfi<sup>3</sup>, G. Anton<sup>4</sup>, M. Ardid<sup>5</sup>, J.-J. Aubert<sup>6</sup>, T. Avgitas<sup>7</sup>,  
B. Baret<sup>7</sup>, J. Barrios-Martí<sup>8</sup>, S. Basa<sup>9</sup>, B. Belhorma<sup>10</sup>, V. Bertin<sup>6</sup>, S. Biagi<sup>11</sup>, R. Bormuth<sup>12,13</sup>,  
S. Bourret<sup>7</sup>, M.C. Bouwhuis<sup>12</sup>, H. Brânzaş<sup>14</sup>, R. Bruijn<sup>12,15</sup>, J. Brunner<sup>6</sup>, J. Busto<sup>6</sup>,  
A. Capone<sup>16,17</sup>, L. Caramete<sup>14</sup>, J. Carr<sup>6</sup>, S. Celli<sup>16,17,18</sup>, R. Cherkaoui El Moursli<sup>19</sup>, T. Chiarusi<sup>20</sup>,  
M. Circella<sup>21</sup>, J.A.B. Coelho<sup>7</sup>, A. Coleiro<sup>7,8</sup>, R. Coniglione<sup>11</sup>, H. Costantini<sup>6</sup>, P. Coyle<sup>6</sup>,  
A. Creusot<sup>7</sup>, A. F. Díaz<sup>22</sup>, A. Deschamps<sup>23</sup>, G. De Bonis<sup>16</sup>, C. Distefano<sup>11</sup>, I. Di Palma<sup>16,17</sup>,  
A. Domi<sup>3,24</sup>, C. Donzaud<sup>7,25</sup>, D. Dornic<sup>6</sup>, D. Drouhin<sup>1</sup>, T. Eberl<sup>4</sup>, I. El Bojaddaini<sup>26</sup>, N. El  
Khayati<sup>19</sup>, D. Elsässer<sup>27</sup>, A. Enzenhöfer<sup>6</sup>, A. Ettahiri<sup>19</sup>, F. Fassi<sup>19</sup>, I. Felis<sup>5</sup>, L.A. Fusco<sup>20,28</sup>,  
P. Gay<sup>29,7</sup>, V. Giordano<sup>30</sup>, H. Glotin<sup>31,32</sup>, T. Grégoire<sup>7</sup>, R. Gracia Ruiz<sup>7,33</sup>, K. Graf<sup>4</sup>,  
S. Hallmann<sup>4</sup>, H. van Haren<sup>34</sup>, A.J. Heijboer<sup>12</sup>, Y. Hello<sup>23</sup>, J.J. Hernández-Rey<sup>8</sup>, J. Höfl<sup>4</sup>,  
J. Hofestädt<sup>4</sup>, C. Hugon<sup>3,24</sup>, G. Illuminati<sup>8</sup>, C.W. James<sup>4</sup>, M. de Jong<sup>12,13</sup>, M. Jongen<sup>12</sup>,  
M. Kadler<sup>27</sup>, O. Kalekin<sup>4</sup>, U. Katz<sup>4</sup>, D. Kießling<sup>4</sup>, A. Kouchner<sup>7,32</sup>, M. Kreter<sup>27</sup>,  
I. Kreykenbohm<sup>35</sup>, V. Kulikovskiy<sup>6,36</sup>, C. Lachaud<sup>7</sup>, R. Lahmann<sup>4</sup>, D. Lefèvre<sup>37</sup>, E. Leonora<sup>30,38</sup>,  
M. Lotze<sup>8</sup>, S. Loucatos<sup>39,7</sup>, M. Marcelin<sup>9</sup>, A. Margiotto<sup>20,28</sup>, A. Marinelli<sup>40,41</sup>,  
J.A. Martínez-Mora<sup>5</sup>, R. Mele<sup>42,43</sup>, K. Melis<sup>12,15</sup>, T. Michael<sup>12</sup>, P. Migliozi<sup>42</sup>, A. Moussa<sup>26</sup>,  
S. Navas<sup>44</sup>, E. Nezri<sup>9</sup>, M. Organokov<sup>33</sup>, G.E. Pāvālaš<sup>14</sup>, C. Pellegrino<sup>20,28</sup>, C. Perrina<sup>16,17</sup>,  
P. Piattelli<sup>11</sup>, V. Popa<sup>14</sup>, T. Pradier<sup>33</sup>, L. Quinn<sup>6</sup>, C. Racca<sup>1</sup>, G. Riccobene<sup>11</sup>, A. Sánchez-Losa<sup>21</sup>,  
M. Saldaña<sup>5</sup>, I. Salvadori<sup>6</sup>, D. F. E. Samtleben<sup>12,13</sup>, M. Sanguineti<sup>3,24</sup>, P. Sapienza<sup>11</sup>,  
F. Schüssler<sup>39</sup>, C. Sieger<sup>4</sup>, M. Spurio<sup>20,28</sup>, Th. Stolarczyk<sup>39</sup>, M. Taiuti<sup>3,24</sup>, Y. Tayalati<sup>19</sup>,  
A. Trovato<sup>11</sup>, D. Turpin<sup>6</sup>, C. Tönnes<sup>8</sup>, B. Vallage<sup>39,7</sup>, V. Van Elewyck<sup>7,32</sup>, F. Versari<sup>20,28</sup>,  
D. Vivolo<sup>42,43</sup>, A. Vizzoca<sup>16,17</sup>, J. Wilms<sup>35</sup>, J.D. Zornoza<sup>8</sup>, J. Zúñiga<sup>8</sup>.

<sup>1</sup>GRPHE - Université de Haute Alsace - Institut universitaire de technologie de Colmar, 34 rue du Grillenbreit BP 50568 - 68008 Colmar, France

<sup>2</sup>Technical University of Catalonia, Laboratory of Applied Bioacoustics, Rambla Exposició, 08800 Vilanova i la Geltrú, Barcelona, Spain

<sup>3</sup>INFN - Sezione di Genova, Via Dodecaneso 33, 16146 Genova, Italy

<sup>4</sup>Friedrich-Alexander-Universität Erlangen-Nürnberg, Erlangen Centre for Astroparticle Physics, Erwin-Rommel-Str. 1, 91058 Erlangen, Germany

<sup>5</sup>Institut d'Investigació per a la Gestió Integrada de les Zones Costaneres (IGIC) - Universitat Politècnica de València. C/ Paranimf 1, 46730 Gandia, Spain

<sup>6</sup>Aix Marseille Univ, CNRS/IN2P3, CPPM, Marseille, France

<sup>7</sup>APC, Univ Paris Diderot, CNRS/IN2P3, CEA/Irfu, Obs de Paris, Sorbonne Paris Cité, France

<sup>8</sup>IFIC - Instituto de Física Corpuscular (CSIC - Universitat de València) c/ Catedrático José Beltrán, 2 E-46980 Paterna, Valencia, Spain

<sup>9</sup>LAM - Laboratoire d'Astrophysique de Marseille, Pôle de l'Étoile Site de Château-Gombert, rue Frédéric Joliot-Curie 38, 13388 Marseille Cedex 13, France

<sup>10</sup>National Center for Energy Sciences and Nuclear Techniques, B.P.1382, R. P.10001 Rabat, Morocco

<sup>11</sup>INFN - Laboratori Nazionali del Sud (LNS), Via S. Sofia 62, 95123 Catania, Italy

- <sup>12</sup>Nikhef, Science Park, Amsterdam, The Netherlands
- <sup>13</sup>Huygens-Kamerlingh Onnes Laboratorium, Universiteit Leiden, The Netherlands
- <sup>14</sup>Institute of Space Science, RO-077125 Bucharest, Măgurele, Romania
- <sup>15</sup>Universiteit van Amsterdam, Instituut voor Hoge-Energie Fysica, Science Park 105, 1098 XG Amsterdam, The Netherlands
- <sup>16</sup>INFN - Sezione di Roma, P.le Aldo Moro 2, 00185 Roma, Italy
- <sup>17</sup>Dipartimento di Fisica dell'Università La Sapienza, P.le Aldo Moro 2, 00185 Roma, Italy
- <sup>18</sup>Gran Sasso Science Institute, Viale Francesco Crispi 7, 00167 L'Aquila, Italy
- <sup>19</sup>University Mohammed V in Rabat, Faculty of Sciences, 4 av. Ibn Battouta, B.P. 1014, R.P. 10000 Rabat, Morocco
- <sup>20</sup>INFN - Sezione di Bologna, Viale Berti-Pichat 6/2, 40127 Bologna, Italy
- <sup>21</sup>INFN - Sezione di Bari, Via E. Orabona 4, 70126 Bari, Italy
- <sup>22</sup>Department of Computer Architecture and Technology/CITIC, University of Granada, 18071 Granada, Spain
- <sup>23</sup>Géozur, UCA, CNRS, IRD, Observatoire de la Côte d'Azur, Sophia Antipolis, France
- <sup>24</sup>Dipartimento di Fisica dell'Università, Via Dodecaneso 33, 16146 Genova, Italy
- <sup>25</sup>Université Paris-Sud, 91405 Orsay Cedex, France
- <sup>26</sup>University Mohammed I, Laboratory of Physics of Matter and Radiations, B.P.717, Oujda 6000, Morocco
- <sup>27</sup>Institut für Theoretische Physik und Astrophysik, Universität Würzburg, Emil-Fischer Str. 31, 97074 Würzburg, Germany
- <sup>28</sup>Dipartimento di Fisica e Astronomia dell'Università, Viale Berti Pichat 6/2, 40127 Bologna, Italy
- <sup>29</sup>Laboratoire de Physique Corpusculaire, Clermont Université, Université Blaise Pascal, CNRS/IN2P3, BP 10448, F-63000 Clermont-Ferrand, France
- <sup>30</sup>INFN - Sezione di Catania, Viale Andrea Doria 6, 95125 Catania, Italy
- <sup>31</sup>LSIS, Aix Marseille Université CNRS ENSAM LSIS UMR 7296 13397 Marseille, France; Université de Toulon CNRS LSIS UMR 7296, 83957 La Garde, France
- <sup>32</sup>Institut Universitaire de France, 75005 Paris, France
- <sup>33</sup>Université de Strasbourg, CNRS, IPHC UMR 7178, F-67000 Strasbourg, France
- <sup>34</sup>Royal Netherlands Institute for Sea Research (NIOZ) and Utrecht University, Landsdiep 4, 1797 SZ 't Horntje (Texel), the Netherlands
- <sup>35</sup>Dr. Reimis-Sternwarte and ECAP, Friedrich-Alexander-Universität Erlangen-Nürnberg, Sternwartstr. 7, 96049 Bamberg, Germany
- <sup>36</sup>Moscow State University, Skobeltsyn Institute of Nuclear Physics, Leninskie gory, 119991 Moscow, Russia
- <sup>37</sup>Mediterranean Institute of Oceanography (MIO), Aix-Marseille University, 13288, Marseille, Cedex 9, France; Université du Sud Toulon-Var, CNRS-INSU/IRD UM 110, 83957, La Garde Cedex, France
- <sup>38</sup>Dipartimento di Fisica ed Astronomia dell'Università, Viale Andrea Doria 6, 95125 Catania, Italy
- <sup>39</sup>Direction des Sciences de la Matière - Institut de recherche sur les lois fondamentales de l'Univers - Service de Physique des Particules, CEA Saclay, 91191 Gif-sur-Yvette Cedex, France
- <sup>40</sup>INFN - Sezione di Pisa, Largo B. Pontecorvo 3, 56127 Pisa, Italy
- <sup>41</sup>Dipartimento di Fisica dell'Università, Largo B. Pontecorvo 3, 56127 Pisa, Italy
- <sup>42</sup>INFN - Sezione di Napoli, Via Cintia 80126 Napoli, Italy
- <sup>43</sup>Dipartimento di Fisica dell'Università Federico II di Napoli, Via Cintia 80126, Napoli, Italy
- <sup>44</sup>Dpto. de Física Teórica y del Cosmos & C.A.F.P.E., University of Granada, 18071 Granada, Spain

**Acknowledgements:**

The authors acknowledge the financial support of the funding agencies: Centre National de la Recherche Scientifique (CNRS), Commissariat à l'énergie atomique et aux énergies alternatives (CEA), Commission Européenne (FEDER fund and Marie Curie Program), Institut Universitaire de France (IUF), IdEx program and UnivEarthS Labex program at Sorbonne Paris Cité (ANR-10-LABX-0023 and ANR-11-IDEX-0005-02), Labex OCEVU (ANR-11-LABX-0060) and the A\*MIDEX project (ANR-11-IDEX-0001-02), Région Île-de-France (DIM-ACAV), Région Alsace (contrat CPER), Région Provence-Alpes-Côte d'Azur, Département du Var and Ville de La Seyne-sur-Mer, France; Bundesministerium für Bildung und Forschung (BMBF), Germany; Istituto Nazionale di Fisica Nucleare (INFN), Italy; Stichting voor Fundamenteel Onderzoek der Materie (FOM), Nederlandse organisatie voor Wetenschappelijk Onderzoek (NWO), the Netherlands; Council of the President of the Russian Federation for young scientists and leading scientific schools supporting grants, Russia; National Authority for Scientific Research (ANCS), Romania; Ministerio de Economía y Competitividad (MINECO): Plan Estatal de Investigación (refs. FPA2015-65150-C3-1-P, -2-P and -3-P, (MINECO/FEDER)), Severo Ochoa Centre of Excellence and MultiDark Consolider (MINECO), and Prometeo and Grisolia programs (Generalitat Valenciana), Spain; Ministry of Higher Education, Scientific Research and Professional Training, Morocco. We also acknowledge the technical support of Ifremer, AIM and Foselev Marine for the sea operations and the CC-IN2P3 for the computing facilities.

## New Constraints on all flavour Galactic diffuse neutrino emission with the ANTARES telescope.

---

**Timothée Grégoire**

*APC, 10 rue Alice Domon et Lenonie Duquet, 75013 Paris , France*

*E-mail: [tgregoir@apc.in2p3.fr](mailto:tgregoir@apc.in2p3.fr)*

**Bruny Baret\***

*APC, 10 rue Alice Domon et Lenonie Duquet, 75013 Paris , France*

*E-mail: [baret@in2p3.fr](mailto:baret@in2p3.fr)*

**on behalf of the ANTARES collaboration.**

The characterization of the high energy neutrino flux from interaction of galactic Cosmic Rays with interstellar matter during their diffusion could shed a new light on Galactic accelerator features, gas distribution morphology and Galactic cosmic ray transport. The central Galactic plane can host an enhanced neutrino production, thus leading to anisotropies in the extraterrestrial neutrino signal as measured by the IceCube Collaboration. The ANTARES neutrino telescope, located in the Mediterranean Sea, offers a favourable view on this part of the sky, thereby allowing for a contribution to the determination of this flux. The expected diffuse Galactic neutrino emission can be obtained linking a model of generation and propagation of cosmic rays with the morphology of the gas distribution in the Milky Way. In this paper, the newly introduced so-called “Gamma model” is assumed as reference. Considering a radially-dependent diffusion coefficient, this model accounts for local cosmic ray measurements, as well as Galactic gamma ray observations. Nine years of ANTARES data are used in this work to search for a possible Galactic contribution to the IceCube neutrino signal. All flavour neutrino interactions are considered, using events with either a track or shower signature. No excess of events is observed and an upper limit is set on the neutrino flux of 1.2 – 1.1 times the prediction of the “Gamma model” depending on the cosmic ray spectrum cut-off. This limit excludes the diffuse Galactic neutrino emission as the major cause of the “spectral anomaly” between the two hemispheres measured by IceCube.

*35th International Cosmic Ray Conference - ICRC2017 -*

*10-20 July, 2017*

*Bexco, Busan, Korea*

---

\*Speaker.

## 1. Introduction

The measured diffuse high-energy gamma ray emission along the Galactic plane by the Fermi-LAT telescope [1] can be attributed above a few GeV to photons produced in neutral pion decays coming from primary cosmic ray (CR) interactions with the ambient medium (dust, molecular clouds, etc.). A neutrino counterpart emission is also expected from  $\pi^{+/-}$  decays. The large coverage of the Southern Hemisphere by the ANTARES neutrino telescope, as well as its large effective area and good angular resolution, allows to test this hypothesis. The model “KRA $\gamma$ ” or “Gamma model” used in this paper relies on radially-dependant CR diffusion and reproduces local CR features, as well as the diffuse Galactic gamma ray emission measured by Fermi-LAT, H.E.S.S. and Milagro experiments [2, 3]. It predicts an expected full sky neutrino flux induced by Galactic CR interactions up to five times higher in the central galactic part than previous models [4]. Consistently with KASCADE-Grande observations [5], two different energy cut-offs of primary CR protons, at 5 and 50 PeV respectively, have been considered. They will be referred to as the two “reference models” in this article.

In the last few years, the IceCube Collaboration has reported a significant excess of high-energy neutrinos with respect to the expected atmospheric background [6, 7, 8]. The spectral energy distribution obtained with 4 years of “high-energy starting events” (HESE) through a full sky analysis results in a one flavour normalisation factor  $E^2\Phi(E) = 2.2(\pm 0.7) \cdot (E/100 \text{ TeV})^{-0.58} \times 10^{-8} \text{ GeV cm}^{-2} \text{ s}^{-1} \text{ sr}^{-1}$  with a fitted spectral index  $\alpha = 2.58 \pm 0.25$  [7]. Nevertheless, a dedicated analysis with 6 years of muonic neutrinos from the Northern Hemisphere shows a normalisation factor of  $E^2\Phi(E) = 0.90^{+0.3}_{-0.27} \cdot (E/100 \text{ TeV})^{-0.13} \times 10^{-8} \text{ GeV cm}^{-2} \text{ s}^{-1} \text{ sr}^{-1}$  and a spectral index  $\alpha = 2.13 \pm 0.13$  [9] generating a non-negligible tension between the measured neutrino spectral energy distributions of the two hemispheres, the so-called “spectral anomaly”.

As the central region of the Milky Way is at negative declinations, the sum of a Galactic and an extragalactic component [10, 11] can result in different spectral behaviours in the two hemispheres.

The ANTARES view of the Southern Sky and its very good angular resolution makes it well suited to either detect the neutrino flux predicted by the reference models or place competitive upper limits. A maximum likelihood analysis is performed assuming the angular and energy distribution of the corresponding signal events and a new stringent upper limit is obtained on the neutrino flux over three decades in energy based on 9 years of data taking.

## 2. The ANTARES detector and data sample

The ANTARES neutrino telescope [12] is installed at 2475 m depth in the Mediterranean sea, 40 km off the coast of Toulon, France. Two detection channels are available for neutrinos above a few tens of GeV: charged current interactions of muonic neutrinos, with the subsequent Cherenkov emission by the outgoing muon, the so-called “track events”; all other interactions, producing electromagnetic or hadronic showers in the detector, lead to so-called “shower events”. The former, have a sub-degree angular resolution, an energy reconstruction accuracy of the order of a fraction of a decade and benefit from the kilometer-scale muon track length which enlarges the effective detection. The latter type of events has an angular accuracy of a few degrees and

an energy resolution of 10% but these performances are achievable only in a smaller effective detection volume.

The data used in this search have been recorded between the 29th of January 2007 and the 31st of December 2015 for a total livetime of 2423.6 days.

The procedure for suppressing the misreconstructed atmospheric muons and select a sample of Earth through-going neutrino candidates events follows the one used for the search of point-like sources in [13]. The selection of events in this analysis maximizes the detection power of the flux predicted by the reference model with a 50 PeV cut-off. The dataset consists of 7300 tracks and 208 showers

### 3. Search Method

This analysis relies on a likelihood ratio test, similar to the one used in the search for neutrinos from individual point-like or extended sources by ANTARES [14, 15, 16, 17]. It is adapted here to a full-sky search where the signal map is built according to the reference models mentioned above. A probability density function of observables was defined according to given expectations/models. Data are considered to be a mixture of signal and background events, so the likelihood function is defined as:

$$\mathcal{L}_{\text{sig+bkg}} = \prod_{\mathcal{T} \in \{\text{tr,sh}\}} \prod_{i \in \mathcal{T}} \mu_{\text{sig}}^{\mathcal{T}} \cdot pdf_{\text{sig}}^{\mathcal{T}}(E_i, \alpha_i, \delta_i) + \mu_{\text{bkg}}^{\mathcal{T}} \cdot pdf_{\text{bkg}}^{\mathcal{T}}(E_i, \theta_i, \delta_i) \quad (3.1)$$

where  $E_i$  is the reconstructed energy,  $\alpha_i$  and  $\delta_i$  right ascension and declination (equatorial coordinates), and  $\theta_i$  zenith angle of the event  $i$ . For each event topology  $\mathcal{T}$  (track or shower), given a total number of events  $\mu_{\text{tot}}^{\mathcal{T}}$ , the number of background events  $\mu_{\text{bkg}}^{\mathcal{T}}$  corresponds to  $\mu_{\text{tot}}^{\mathcal{T}} - \mu_{\text{sig}}^{\mathcal{T}}$ . The number of signal events  $\mu_{\text{sig}}^{\mathcal{T}}$  is fitted when maximising the likelihood, allowing only non-negative values. The signal and background probability density functions of an event are defined as:

$$pdf_{\text{sig}}^{\mathcal{T}}(E_i, \alpha_i, \delta_i) = \mathcal{M}_{\text{sig}}^{\mathcal{T}}(\alpha_i, \delta_i) \cdot \mathcal{E}_{\text{sig}}^{\mathcal{T}}(E_i, \alpha_i, \delta_i) \quad (3.2)$$

$$pdf_{\text{bkg}}^{\mathcal{T}}(E_i, \theta_i, \delta_i) = \mathcal{M}_{\text{bkg}}^{\mathcal{T}}(\delta_i) \cdot \mathcal{E}_{\text{bkg}}^{\mathcal{T}}(E_i, \theta_i) \quad (3.3)$$

where  $\mathcal{M}^{\mathcal{T}}$  are the probability density functions of an event to be reconstructed in a given position in the sky. The probability density functions  $\mathcal{M}_{\text{sig}}^{\mathcal{T}}$ , shown in Figure 1 (for the 5 PeV energy cut-off model) obtained from Monte Carlo simulation, depend on the differential neutrino fluxes predicted by the reference models folded with the detector response to a given direction in the sky. The background distribution  $\mathcal{M}_{\text{bkg}}^{\mathcal{T}}$  is based on data and only depends on declination since the atmospheric background right ascension distribution is flat because of the Earth's rotation and of the uniform data taking along a sidereal day. The probability density function of the reconstructed energy for the signal,  $\mathcal{E}_{\text{sig}}^{\mathcal{T}}$  depends on equatorial coordinates as does the energy spectra of the reference models. For the background,  $\mathcal{E}_{\text{bkg}}^{\mathcal{T}}$  depends on the corresponding local zenith  $\theta_i$  to account for potential reconstruction systematic effects due to the detector response.

The test statistic  $\mathcal{Q}$  is then defined as the logarithm of the likelihood ratio:

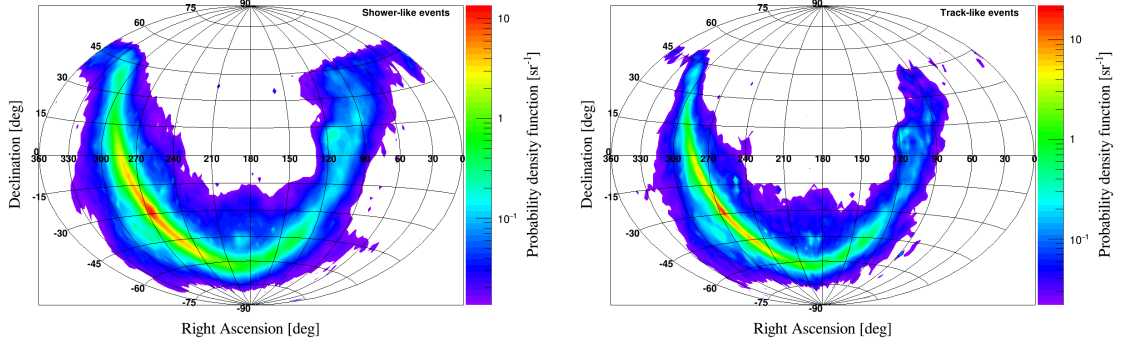


Figure 1: Probability density function of the reconstructed direction of signal events  $\mathcal{M}_{\text{sig}}^{\mathcal{T}}$ , in equatorial coordinates for shower-like (left) and track-like (right) events.

$$\mathcal{Q} = \log_{10}(\mathcal{L}_{\text{sig+bkg}}) - \log_{10}(\mathcal{L}_{\text{bkg}}) \quad (3.4)$$

with  $\mathcal{L}_{\text{bkg}} = \mathcal{L}_{\text{sig+bkg}}(\mu_{\text{sig}}^{\text{sh}} = \mu_{\text{sig}}^{\text{tr}} = 0)$ .

The detection power is computed by building the probability density functions of the test statistic  $pdf_{\Phi}(\mathcal{Q})$  for different normalisation factors  $\Phi$  of the reference model fluxes. Pseudo-experiments are thus produced, varying the number of signal events  $\mu_{\text{sig}}^{\text{sh+tr}}$  accordingly. They are generated using the probability density functions  $\mathcal{M}^{\mathcal{T}}$  and  $\mathcal{E}^{\mathcal{T}}$  defined before. A total of  $10^5$  pseudo-experiments are generated for the background ( $\mu_{\text{sig}}^{\text{sh+tr}} = 0$ ) and  $10^4$  for each value of  $\mu_{\text{sig}}^{\text{sh+tr}}$  in the range [1,55] where the rate of showers, taken from the Monte Carlo simulation, is  $\sim 20\%$  of  $\mu_{\text{sig}}^{\text{sh+tr}}$ . For each pseudo-experiment, the number of fitted track ( $\mu_{\text{fit}}^{\text{tr}}$ ) and shower ( $\mu_{\text{fit}}^{\text{sh}}$ ) events is recorded. The distribution of  $[\mu_{\text{sig}}^{\text{sh+tr}} - (\mu_{\text{fit}}^{\text{tr}} + \mu_{\text{fit}}^{\text{sh}})]$  has null mean value and a standard deviation  $\sigma^* = 13$  for the model with the 5 PeV cut-off and  $\sigma^* = 12$  with the 50 PeV cut-off. It is worth noticing that the value of  $\sigma^*$  is related to the background fluctuation, which does not change when varying the true number of signal events for a given model. The probability density functions of  $\mathcal{Q}$  for integer numbers of signal events  $pdf_{\mu_{\text{sig}}^{\text{sh+tr}}}(\mathcal{Q})$  are obtained from pseudo-experiments. They are linked to  $pdf_{\Phi}(\mathcal{Q})$ , with  $\Phi$  leading to a mean number of detected signal events  $n$ , by:

$$pdf_{\Phi}(\mathcal{Q}) = \sum_{\mu_{\text{sig}}^{\text{sh+tr}}} P(\mu_{\text{sig}}^{\text{sh+tr}}|n) \cdot pdf_{\mu_{\text{sig}}^{\text{sh+tr}}}(\mathcal{Q}) \quad (3.5)$$

where  $P$  is the Poissonian probability distribution.

The systematic uncertainty on the acceptance of the ANTARES photomultipliers implies an uncertainty on the effective area of 15% [21]. To account for this, the number of expected signal events  $n$  from a given flux is fluctuated using a Gaussian distribution with a standard deviation of 15%. An uncertainty on the background distribution due to statistical fluctuations in the data is also taken into account by fluctuating  $\mathcal{M}_{\text{bkg}}^{\mathcal{T}}(\delta_i)$ .

The p-value of a given  $\mathcal{Q}$  is defined as the probability to measure a test statistic larger than this one in the background only case. It is given by the anti-cumulative probability density function of  $\mathcal{Q}$  with no injected signal (Figure 2). Upper limits at a given confidence level are set according to the corresponding distributions with injected signal events.



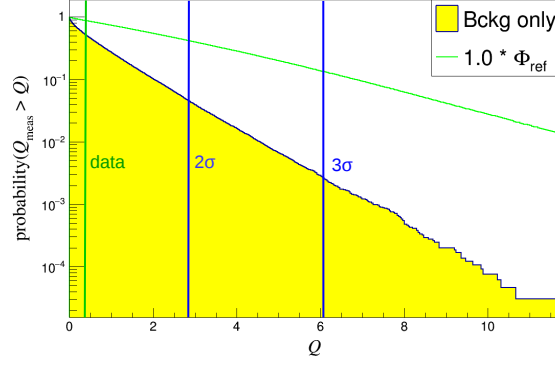


Figure 2: Anti-cumulative distribution of the test statistic  $\mathcal{Q}$  from pseudo-experiments for background only (yellow area) and with signal from the reference model with the 5 PeV cut-off (red line). The corresponding values of the test statistic for  $2\sigma$  and  $3\sigma$  confidence level are shown (blue lines) along with the value obtained with data (green line).

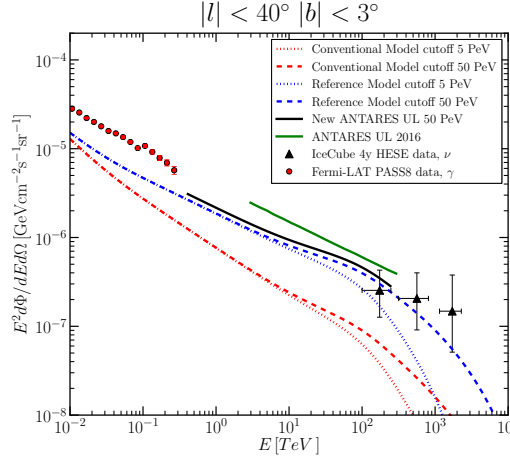


Figure 3: ANTARES upper limit at 90% confidence level on the three flavour neutrino flux (solid black line) on the reference model with a 50 PeV energy cut-off (blue dashed line). The neutrino fluxes according to the reference model with the 5 PeV energy cut-off (blue dotted line), the conventional model with the 50 PeV (red dashed line) and 5 PeV (red dotted line) cut-offs are shown for all

For the model with the 5 PeV cut-off, 90% of signal events are in the energy range [0.35,130] TeV for track-like events and between [2.0,150] TeV for shower-like events. For the 50 PeV cut-off, these energy ranges are [0.40,230] TeV for the tracks and [2.2,260] TeV for the showers. To avoid biasing the analysis, the data have been blinded by time-scrambling. Both the sensitivity and the discovery power of the analysis are derived from this blinded dataset. The sensitivity, defined as the average upper limit at 90% confidence level, is  $1.4 \times \Phi_{\text{ref}}$  when a cut-off for CR primary protons at 5 PeV is set. A mean of  $\mu^* = 11.6$  signal events is expected from the model. It corresponds to the

Energy cut-off	$\mu^*$	$\sigma^*$	$\mu_{\text{data}}^{\text{sh}}$	$\mu_{\text{data}}^{\text{tr}}$	p-value	UL at 90% CL
5 PeV	11.6	13	1.9	$2 \times 10^{-3}$	0.67	$1.1 \times \Phi_{\text{ref}}$
50 PeV	13.7	12	2.6	$7 \times 10^{-4}$	0.54	$1.2 \times \Phi_{\text{ref}}$

Table 1: Results of the presented analysis for the two reference models corresponding to different energy cut-offs. The number of expected signal events,  $\mu^*$ , is shown, as well as  $\sigma^*$ , the standard deviation of the distribution of the difference between the number of fitted events and the number of injected events in the pseudo-experiment. For the data sample, the numbers of fitted shower-like events,  $\mu_{\text{data}}^{\text{sh}}$ , and track-like events,  $\mu_{\text{data}}^{\text{tr}}$ , are reported with the p-values and the upper limits at 90% confidence level.

sum of track-like and shower-like events, showers constituting  $\sim 20\%$  of the total. The resulting discovery power at  $3\sigma$  confidence level is 7%. For the model with a 50 PeV cut-off, the sensitivity is  $1.05 \times \Phi_{\text{ref}}$  and  $\mu^* = 13.7$  signal events are expected, resulting in a discovery power of 14% for a  $3\sigma$  confidence level.

#### 4. Results

After unblinding, the test statistic of the data is computed. The corresponding  $\mathcal{Q}$  value is shown as the green line in Figure 2. Table 1 presents the results for the two different cut-off energies (column 1) considered by the models. Column 2 reports the number of expected events,  $\mu^*$ , and column 3 the standard deviation of the distribution of the number of fitted events,  $\sigma^*$ , which are defined in section 3.

For the data sample, the numbers of fitted track-like events,  $\mu_{\text{data}}^{\text{tr}}$ , and shower-like events,  $\mu_{\text{data}}^{\text{sh}}$ , are reported in columns 4 and 5, respectively. Their sum is smaller than  $\mu^*$ , but still compatible with the expected fluctuations. These include the Gaussian fluctuation due to the background (which is within  $1\sigma^*$ ) and the Poissonian fluctuation on the number of signal events.

The p-value of the data – as defined in section 3 – is reported in column 6. The derived upper limits at 90% confidence level on the reference models are reported in the last column of Table 1.

Figure 3 shows the 90% confidence level upper limit of this analysis that relies on the particular morphology and energy spectrum of the reference model. The blue line refers to the reference model assuming a cut-off of 5 PeV for the primary protons producing neutrinos when interacting with gas. Although full sky data were used in this analysis, the expectations and the results concerning the inner Galactic plane region ( $|l| < 40^\circ$  and  $|b| < 3^\circ$ ) are shown on this plot. This allows to compare the improvement of the presented limit with respect to the previous ANTARES constraint on the neutrino emission [18] from the same region. The diffuse gamma-ray spectral energy distribution derived from PASS8 Fermi-LAT data [19] obtained after the subtraction of point-like components comprised in this region is also shown for comparison. In the same way, the red dashed line shows the predicted spectrum from the conventional model with homogeneous CR diffusion. The neutrino flux from individual events with origin compatible with this region coming from the 4 year IceCube HESE catalog is shown as the black triangles. Only all flavour neutrino fluxes are

represented in this figure.

## 5. Conclusions

The study reported here applies a likelihood ratio test on nine years of ANTARES data collected from 2007 to 2015 to search for a diffuse Galactic-dominated neutrino flux, characterised by the recently introduced “Gamma model” used as reference model. As a result, a neutrino flux with normalisation factor of  $1.1 \times \Phi_{\text{ref}}$  (resp.  $1.2 \times \Phi_{\text{ref}}$ ) is excluded at 90% confidence level when the model with the 5 PeV cut-off (resp. 50 PeV) is considered.

Using neutrinos of all flavours as well as a larger amount of data leads to an improvement in the sensitivity and more stringent upper limits with respect to the previous ANTARES analysis [18]. The new upper limits do not extend above  $\sim 200$  TeV due to the significant softening of the spectrum. The additional gain in sensitivity below 3 TeV with respect to the previous analysis results from the usage of a new unbinned method that uses spatial and energy information. At low energies, the limit obtained from this analysis almost reaches the high-energy tail of the Fermi-LAT sensitivity and giving the enhanced Galactic hadronic emission predicted by the reference models with respect to a conventional scenario, the obtained limits represent a strong constraint on a possible diffuse neutrino emission from the Galactic Plane.

Considering the flux upper limit with 90% confidence level shown in Table 1 for the 50 PeV cut-off, at most 18% of the cosmic neutrino events measured by IceCube with the HESE dataset can originate from CR diffusion. This corresponds to about 5.2 out of the 28.6 HESE with energy above 60 TeV expected to be cosmic neutrinos, as reported in [22]. This limit is more restrictive than that allowed in [10, 20]. The reference model produces a larger North/South asymmetry than the conventional scenario: more than  $\sim 80\%$  of the events are expected from the Southern hemisphere. Nevertheless, the contribution of the diffuse Galactic component to the difference between the observed number of HESE arising from the two hemispheres cannot be larger than 3.3 HESE, i.e.  $\sim 10\%$  of the full sky flux. As a result, the neutrino flux produced by the Galactic CR interaction with gas cannot explain by itself the IceCube spectral anomaly. These considerations are even more restrictive for the case of the 90% confidence level upper limit corresponding to a primary CR cut-off of 5 PeV, as evident from the predicted flux in Figure 2.

## References

- [1] M. Ackermann et al. Fermi-LAT Observations of the Diffuse  $\gamma$ -Ray Emission: Implications for Cosmic Rays and the Interstellar Medium. *Astrophys. J.*, 750:3, 2012.
- [2] D. Gaggero, D. Grasso, A. Marinelli, A. Urbano, and M. Valli. The Gamma-Ray and Neutrino Sky: A Consistent Picture of Fermi-LAT, Milagro, and IceCube Results. *Astrophys. J. Lett.*, 815:L25, 2015.
- [3] D. Gaggero, D. Grasso, A. Marinelli, M. Taoso, and A. Urbano. Diffuse cosmic rays shining in the Galactic center: A novel interpretation of H.E.S.S. and Fermi-LAT gamma-ray data. *arXiv:1702.01124*, 2017.

- [4] D. Gaggero, D. Grasso, A. Marinelli, A. Urbano, and M. Valli. A Hadronic Scenario for the Galactic Ridge. *PoS, ICRC2015:1126*, 2015.
- [5] KASCADE-Grande measurements of energy spectra for elemental groups of cosmic rays. *Astropart. Phys.*, 47:54–66, 2013.
- [6] M. G. Aartsen et al. First Observation of PeV-Energy Neutrinos with IceCube. *Phys. Rev. Lett.*, 111(2):021103, 2013.
- [7] M. G. Aartsen et al. The IceCube Neutrino Observatory - Contributions to ICRC 2015 Part II: Atmospheric and Astrophysical Diffuse Neutrino Searches of All Flavors. *arXiv:1510.05223*, 2015.
- [8] M. G. Aartsen et al. Searches for Extended and Point-like Neutrino Sources with Four Years of IceCube Data. *Astrophys. J.*, 796:109, 2014.
- [9] M. G. Aartsen et al. Observation and Characterization of a Cosmic Muon Neutrino Flux from the Northern Hemisphere Using Six Years of IceCube Data. *Astrophys. J.*, 833:3, 2016.
- [10] A. Palladino, M. Spurio, and F. Vissani. On the IceCube spectral anomaly. *J. Cosmol. Astropart. Phys.*, 12:045, 2016.
- [11] A. Marinelli, D. Gaggero, D. Grasso, A. Urbano, and M. Valli. Interpretation of astrophysical neutrinos observed by IceCube experiment by setting Galactic and extra-Galactic spectral components. In *EPJ Web of Conferences*, volume 116, page 04009, 2016.
- [12] M. Ageron et al. ANTARES: The first undersea neutrino telescope. *Nucl. Instrum. Methods A*, 656:11–38, 2011.
- [13] Tino Michael. Neutrino point source search including cascade events with the ANTARES neutrino telescope. *PoS, ICRC2015:1078*, 2016.
- [14] S. Adrián-Martínez et al. Searches for point-like and extended neutrino sources close to the galactic centre using the antares neutrino telescope. *Astrophys. J.*, 786(1):L5, 2014.
- [15] S. Adrián-Martínez et al. The first combined search for neutrino point-sources in the southern hemisphere with the antares and icecube neutrino telescopes. *Astrophys. J.*, 823(1):65, 2016.
- [16] S. Adrián-Martínez et al. Stacked search for time shifted high energy neutrinos from gamma ray bursts with the ANTARES neutrino telescope. *Eur. Phys. J. C*, 77(1), 2017.
- [17] A. Albert et al. Time-dependent search for neutrino emission from x-ray binaries with the ANTARES telescope. *arXiv:1609.07372*, 2016.
- [18] S. Adrián-Martínez et al. Constraints on the neutrino emission from the Galactic Ridge with the ANTARES telescope. *Phys. Lett. B*, 760:143–148, 2016.
- [19] W. Atwood et al. Pass 8: toward the full realization of the Fermi-LAT scientific potential. *arXiv:1303.3514*, 2013.
- [20] A. Neronov and D. Semikoz. Evidence the Galactic contribution to the IceCube astrophysical neutrino flux. *Astropart. Phys.*, 75:60–63, 2016.
- [21] S. Adrian-Martinez et al. Search for Cosmic Neutrino Point Sources with Four Year Data of the ANTARES Telescope. *Astrophys. J.*, 760:53, 2012.
- [22] M. G. Aartsen et al. Searches for Extended and Point-like Neutrino Sources with Four Years of IceCube Data *Astrophys. J.*, 796:109, 2014

## Search for a diffuse flux of cosmic neutrinos with the ANTARES telescope

---

### Thomas Eberl\*

*Friedrich-Alexander-Universität Erlangen-Nürnberg, Erlangen Centre for Astroparticle Physics,  
Erwin-Rommel-Str. 1, 91058 Erlangen, Germany*  
E-mail: [Thomas.Eberl@fau.de](mailto:Thomas.Eberl@fau.de)

### Luigi Antonio Fusco

*INFN - Sezione di Bologna and Dipartimento di Fisica e Astronomia dell'Università di Bologna,  
Viale Berti-Pichat 6/2, 40127 Bologna, Italy*  
E-mail: [luigiantonio.fusco@bo.infn.it](mailto:luigiantonio.fusco@bo.infn.it)

### Sergio Navas

*Departamento de Física Teórica y del Cosmos, Universidad de Granada, Av. Severo Ochoa,  
18071 Granada, Spain.*  
E-mail: [navas@ugr.es](mailto:navas@ugr.es)

### Federico Versari

*INFN - Sezione di Bologna and Dipartimento di Fisica e Astronomia dell'Università di Bologna,  
Viale Berti-Pichat 6/2, 40127 Bologna, Italy*  
E-mail: [federico.versari@bo.infn.it](mailto:federico.versari@bo.infn.it)

### on behalf of the ANTARES Collaboration

The ANTARES detector is the largest neutrino telescope in the Northern hemisphere. Interactions of all neutrino flavours can be observed and reconstructed by the experiment. Events induced by muon neutrino charged-current interactions represent the track channel: the long path travelled by muons before being detected allows to increase the effective detector volume, with excellent angular resolution but limited precision in the event energy reconstruction. The shower channel, i.e. all neutral-current and charged-current interactions of  $\nu_e$  (and possibly  $\nu_\tau$ ) allows for a better energy resolution than the track channel, though only events within a limited fiducial volume can be considered. Exploiting its multi-year dataset, the complementarity of its field of view and its excellent reconstruction performance, ANTARES can independently investigate the cosmic neutrino flux reported by the Antarctic IceCube detector. The latest results of these all-flavour searches for a diffuse astrophysical neutrino flux are presented in this contribution. Using events observed in both channels, an excess of events with respect to the expected atmospheric background is observed with a significance below  $2\sigma$ . Once systematics are included, the corresponding 68% confidence interval encloses the observed IceCube signal.

*35th International Cosmic Ray Conference — ICRC2017  
10–20 July, 2017  
Bexco, Busan, Korea*

---

\*Speaker.

## 1. Introduction

Astrophysical high-energy neutrinos are probes to investigate the origin, the sources and the acceleration mechanisms of primary cosmic rays (CRs). Neutrinos can indeed be produced at the sources of ultra high-energy cosmic rays (UHECRs) and then travel without deflection or absorption over cosmic distances. CRs can produce neutrinos when interacting with the ambient medium via inelastic collisions on nucleons or photons. The former represents the so-called  $pp$  reaction, where a large amount of secondaries is produced, such as short-lived mesons decaying into neutrinos [1]; the latter is described by photo-production processes where the  $p\gamma$  reaction produces a  $\Delta$ -resonance which decays into pions. Neutrinos are produced in the pion decay chain [2]. Under the assumption that neutrinos are produced in meson decays, the neutrino flux at the source is distributed between the three neutrino flavours as  $\nu_e : \nu_\mu : \nu_\tau = 1 : 2 : 0$ . Vacuum oscillations over cosmic distances would produce equipartition in the three flavours at Earth.

A diffuse flux of cosmic neutrinos might originate from either the ensemble of unresolved individual sources, which are too faint to be detected individually, or from the interaction of high-energy CRs as they propagate in the Universe. The observation of a diffuse flux of cosmic neutrinos, i.e. the measurement of its spectrum and flavour composition, could provide valuable information on their production mechanisms. This can be eventually related to the CR acceleration and interaction properties. Under the assumptions made by Waxman and Bahcall [3], the diffuse neutrino flux should follow the same spectrum as that of the parent CRs at the acceleration site, i.e. proportional to  $E^{-2}$  as expected from the Fermi acceleration mechanism [4]. A softer spectrum might originate from extragalactic accelerators that are inside galaxies which are opaque to CRs. This is the case, for example, for starburst galaxies [5] where the matter density is high enough for protons to lose energy before producing pions. The corresponding cosmic neutrino energy spectrum is steeper and lower in normalisation compared to the Waxman and Bahcall prediction.

Searches for a diffuse flux of cosmic neutrinos from the IceCube collaboration have provided the observation of an excess of neutrinos over the expected background [6, 7]. The measured flux can be modelled with single-power-laws  $dN_\nu/dE_\nu = \Phi_0 E_\nu^{-\Gamma}$ , with relatively soft spectral indices ( $\Gamma > 2$ ). Assuming that the astrophysical neutrino flux is isotropic over the whole sky and consisting of equal flavours at Earth, the best-fit spectral index is  $\Gamma = 2.50 \pm 0.09$  and the normalization at 100 TeV is  $\Phi_0^{3f}(100 \text{ TeV}) = 6.7_{-1.2}^{+1.1} \cdot 10^{-18} \text{ GeV}^{-1} \text{ cm}^{-2} \text{ s}^{-1} \text{ sr}^{-1}$  for an all-flavour flux ( $3f$ ) [7]. Always in IceCube, a separate measurement of muons induced by neutrinos coming from the Northern hemisphere [8] yields a best-fit, single-flavour flux  $\Phi_0^{1f}(100 \text{ TeV}) = 9.0_{-2.7}^{+3.0} \cdot 10^{-19} \text{ GeV}^{-1} \text{ cm}^{-2} \text{ s}^{-1} \text{ sr}^{-1}$  and  $\Gamma = 2.13 \pm 0.13$  [8]. This particular channel can access neutrinos only at energies above 100 TeV because of the more abundant atmospheric background from  $\nu_\mu$ -induced events at lower energies, while analyses including  $\nu_e$  and  $\nu_\tau$  interactions have lower energy thresholds. These different measurements of the cosmic neutrino flux by IceCube might be a hint to multiple components in the IceCube signal, such as a hard/extragalactic plus a soft/galactic component [9].

The ANTARES detector [10] can provide valuable information for the identification of this signal. This is especially true if part of this signal has a Galactic origin. This possible component is indeed expected to be more intense at lower energies with respect to the predictions for extragalactic fluxes. Because of its lower energy threshold, ANTARES can study in detail this flux either in

searches for point-like sources [11] or in extended region searches, such as for a contribution of neutrinos coming from CR propagation and interactions in the Milky Way [12].

Previous searches for a diffuse flux of cosmic neutrinos with ANTARES data did not observe any significant excess over the atmospheric background expectations [13, 14, 15, 16]. The analysis presented in this contribution extends the previously analysed data sample and uses events from interactions of all neutrino flavours, which improves the sensitivity of the analysis. As a result, an excess of events over the expected atmospheric backgrounds is observed; though this excess is compatible with the background within its uncertainties, it is also compatible with the expectations from a cosmic contribution to the overall event rate.

## 2. The ANTARES detector and data sample

The ANTARES underwater neutrino telescope [10] is located 40 km off the Southern coast of France in the Mediterranean Sea ( $42^{\circ} 48' \text{ N}$ ,  $6^{\circ} 10' \text{ E}$ ). It consists of a three-dimensional array of 10-inch photomultiplier tubes (PMTs) distributed along 12 vertical lines, anchored to the sea-bed at a depth of about 2500 m and kept taut by a top buoy. Each line includes 75 PMTs distributed in 25 storeys and facing  $45^{\circ}$  downwards. ANTARES is currently the largest and longest operating under-sea neutrino telescope and the largest neutrino experiment in the Northern Hemisphere.

Cherenkov light is induced in the medium by relativistic charged particles produced in the neutrino interaction. Cherenkov photons impinging on the PMTs produce signals (“hits”) which are collected by the experiment. The position, time and collected charge of the hits are used to infer the direction and energy of the incident neutrino. The event-wise information is reconstructed starting from the hit information. Events induced by charged-current (CC) interactions of muon neutrinos produce a track signature in the detector; the long extension of the track enlarges the effective volume of the detector, increasing the event rate. For these events a median angular resolution of  $0.4^{\circ}$  is achieved [11, 17], though the limited information on the whole event limits the energy resolution [18]. On the other hand, all-flavour neutral-current (NC) and CC  $\nu_e$  and  $\nu_{\tau}$  interactions produce electromagnetic and hadronic showers in the instrumented volume. These events can be properly reconstructed with ANTARES [19] only in a restricted fiducial volume, showing a median angular resolution of the order of  $3^{\circ}$  and an excellent energy resolution of about 10%.

ANTARES data, collected from 2007 to 2015, are used in this analysis to search for an excess of cosmic neutrinos over the atmospheric backgrounds. This data sample corresponds to an equivalent livetime of 2450 days, extending the livetime of all previous diffuse-flux analyses performed with ANTARES data by more than a factor of two. Monte Carlo simulations are used to define the event selection. Since data acquisition conditions in the sea environment are not stable in time, dedicated simulations reproduce the time-dependent behaviour of the data taking [20]. Thus, for each data acquisition run, a corresponding Monte Carlo file is generated. A *blinding* policy is followed for the analysis: 10% of the collected data is used to check the agreement between data and Monte Carlo in order to avoid biases in the event selection that could otherwise arise from looking directly at data.



### 3. Search method

The strategy to search for a diffuse flux of cosmic neutrinos can be summarised as a two-step procedure: at first the largely overabundant background of atmospheric muons is reduced by applying cuts on the direction and the quality of the reconstruction output; then, taking advantage of the different spectral behaviour of signal and atmospheric neutrino background, an energy-related cut is applied to improve the signal-to-noise ratio. As mentioned before, equipartition in the three neutrino flavours, as well as between neutrinos and anti-neutrinos, is assumed. In addition, an isotropic flux over the whole sky is considered. Single-power-law energy spectra are used to describe cosmic neutrino fluxes. In this work two options have been considered:  $\Gamma = 2.0$  and  $\Gamma = 2.5$ , close to the best-fit options for the IceCube cosmic signal.

The most abundant background in the search for neutrinos stems from atmospheric downward-going muons reaching the apparatus. The MUPAGE [21, 22] simulation code is used to produce large Monte Carlo samples of atmospheric muon bundles to study this background. The Earth can be used as a shield to reduce the influence of these muons, by rejecting events reconstructed as downward-going. Nonetheless, a certain amount of atmospheric muon events could still be misreconstructed as upward-going. A selection on the event reconstruction quality allows to reduce their influence.

Atmospheric neutrinos are produced together with muons, and they cannot be shielded by the Earth. At high energies, two spectral components contribute to the total atmospheric neutrino flux, namely the *conventional* and the *prompt* components. The conventional flux consists of neutrinos produced in the decays of pions and kaons, more abundant but softer in spectrum; the prompt neutrino component is expected to originate from the decays of charmed hadrons in atmospheric particle cascades, thus has a smaller intensity but a harder spectrum. The assumption made here is that the conventional component is described by the *Honda et al.* calculations [23], while the prompt component follows the *Enberg et al.* prescription [24]. Different predictions for conventional and prompt fluxes have been taken into account in the evaluation of systematic effects, as described in section 4. ANTARES data have been already used to measure the atmospheric muon neutrino energy spectrum in [25].

Atmospheric neutrino interactions are topologically indistinguishable from cosmic neutrinos in ANTARES. However, at the highest energies the astrophysical neutrino flux should be more intense and possibly become visible. An energy-related selection is defined to maximize the signal-to-noise ratio, following the Model Rejection Factor (MRF) procedure [26] based on the Feldmann and Cousins upper limit estimation [27].

#### 3.1 Neutrinos inducing tracks

Track-like events are reconstructed through a multi-step procedure based on likelihood fits [17] using PMT hits. The discrimination between downward-going atmospheric muons and high-energy neutrino-induced events is accomplished by selecting events with a low angular error estimate ( $\beta$ ) and good track-fit quality parameter ( $\Lambda$ ), as well as a large number of hits correlated with the reconstructed track ( $N_{hit}$ ). An *a priori* cut on the reconstructed zenith angle ( $\theta^{track} > 90^\circ$ ) is applied to remove the atmospheric muons which are properly reconstructed as downward-going. Then, a combined cut on  $\Lambda$ ,  $\beta$  and  $N_{hit}$  is used to reject wrongly-reconstructed muons. The optimised cut



corresponds to  $\Lambda > -4.9$ ,  $\beta < 0.5^\circ$  and  $N_{hit} > 35$ ; this reduces by 8 orders of magnitude the number of atmospheric muons in the sample with respect to the overall number of reconstructed events. The resulting atmospheric neutrino rate is of about 1 event/day.

The separation between cosmic and atmospheric neutrinos is achieved by estimating the neutrino energy. Even though this is not directly measurable, the neutrino energy is correlated with the number of photons detected in the event. Higher energy neutrinos produce larger energy deposits in the detector, detectable as additional light, which mostly comes from Cherenkov emission by secondary particles produced in catastrophic energy loss processes along the track. An energy estimator based on Artificial Neural Networks [18] provides the best discrimination between atmospheric and cosmic neutrinos. Figure 1 shows the energy estimator distribution for the selected neutrino sample, also showing the optimal selection cut as from the MRF procedure ( $E_{ANN} > 5$ ) when optimising for a cosmic flux proportional to  $E^{-2}$ ; because of the intense atmospheric muon neutrino background, the optimal selection is almost independent with respect to the spectral behaviour of the cosmic signal.  $13.5 \pm 4$  background events are expected, while 3–3.5 events should be induced by an IceCube-like signal, depending on the spectral index and flux normalisation.

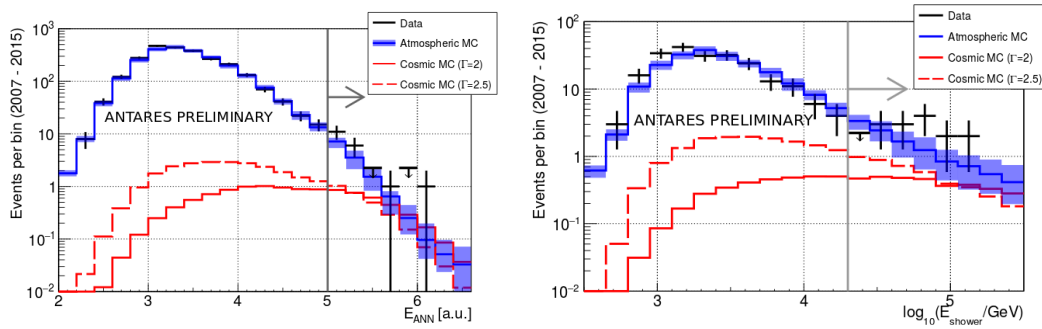


Figure 1: Distribution of the energy estimator for data (black crosses) and Monte Carlo after the event selection cut, before applying the energy-related selection shown as an arrow. Left panel for tracks, right for showers. The blue histograms show atmospheric events, with uncertainties reported by the shaded band (see text for details). Red distributions are for cosmic fluxes with spectral index  $\Gamma=2.0$  (solid) or 2.5 (dashed). The normalisation of the cosmic signal is assumed equal to the best fit from IceCube measurements.

### 3.2 Neutrinos inducing showers

A dedicated reconstruction algorithm has been developed by the ANTARES Collaboration to reconstruct shower-like events [19] with high accuracy in direction and energy. A prefit is firstly performed; this provides the starting point for the final fitting as well as the value of the M-estimator evaluation, which is analogous to a  $\chi^2$  for the hit distribution with respect to the shower hypothesis. This prefit is then followed by a maximum likelihood fit to obtain the shower parameters (direction and energy). The shower signature allows for the proper reconstruction of events only within a fiducial volume; differently from the track-channel, where the long muon track increases the effective volume and thus the event rate at the detector, a smaller number of cascade-like events are detectable in ANTARES. Nonetheless, in this channel, the atmospheric neutrino background is

smaller by more than one order of magnitude, since it is mainly given by electron neutrinos, which are less abundant in atmospheric CR cascades. Finally, the energy resolution achievable for shower-like events allows for a better discrimination between the soft-spectra atmospheric neutrinos and the hard-spectra cosmic ones.

A preliminary event selection procedure, described in [28], is performed vetoing events that are already included in the track analysis, as well as events outside a fiducial volume and with poor reconstruction. After this event selection, the sample is still dominated by atmospheric muons. Three further signal-selecting procedures are defined based on: *a)* the total likelihood that the hit distribution induced by the event comes from an upward-going signal; *b)* the ratio between the likelihood of a track and a shower hypothesis to produce the reconstructed properties given the observed hit distribution; *c)* the ratio between the total measured charge of hits which are “on-time” with respect to the shower hypothesis, i.e. in space/time-correlation with the fitted vertex, and “early” hits arriving before the expectations from a shower hypothesis, thus compatible with a muon propagating through the instrumented volume [19].

The muon-rejecting procedure leaves about 0.008 atmospheric muon events per day in the whole sample. The atmospheric neutrino rate in this channel, after event selection, is approximately 0.1 events/day. The final selection is accomplished by rejecting events with reconstructed shower energy below 20 TeV, as a result of the MRF minimisation. The reconstructed shower energy distribution is reported in Figure 1. Overall, this event selection leads to an estimation of  $10.5 \pm 4$  background events in the whole analysed livetime, when about 4 events are expected from a cosmic signal analogous to the IceCube observation.

#### 4. Results and conclusions

The unblinding of the two samples yielded an observation of 33 (19 tracks and 14 showers) events overall. The expectation from Monte Carlo simulations of the background is 24 events (13.5 tracks and 10.5 showers).

A conservative estimation of the uncertainties on the background yields  $\pm 7$  events. This uncertainty is computed taking into account the uncertainties related to the atmospheric neutrino flux normalisation, both for the conventional and prompt component, as well as on the contribution from different expectations on the behaviour of the primary CR knee [29]. In particular, the conventional flux is free to fluctuate by  $\pm 25\%$ ; the uncertainty on the prompt component is given by the highest and lowest prediction from [24]. It should be noted that the upper limit on the prompt component from IceCube measurement corresponds approximately to the Enberg et al. expectations [8]. The H3a model of the CR energy spectrum and composition is considered in the estimation of the background.

Analogously, the uncertainties on the normalisation of the background from wrongly reconstructed atmospheric muons are taken into account, allowing its normalisation to change by 30%; in addition, as the final number of atmospheric muons in the data sample is extrapolated from Monte Carlo because of the limited statistics, also the uncertainties on this extrapolation are considered. This is completely negligible for the track channel, while it represents the largest contribution for the uncertainties in cascades.

Spectral Index	90% C.L. Upper Limit $\Phi_0^{1f}$ (1 GeV)	68% Confidence Interval $\Phi_0^{1f}$ (1 GeV)	Energy range
2.0	$3.4 \times 10^{-8}$	$0.25 - 2.5 \times 10^{-8}$	40 TeV – 7 PeV
2.5	$1.9 \times 10^{-5}$	$0.14 - 1.4 \times 10^{-5}$	30 TeV – 1.5 PeV

Table 1: 90% C.L. upper limit and 68% confidence interval for the ANTARES diffuse flux analysis of tracks and showers combined, including systematics. The energy range in which the results are valid are computed from MC simulation accounting for the range in which 90% of the signal is contained for each signal spectral index.

Finally, different input for Monte Carlo simulations are considered in order to evaluate the effect of the detector response on the signal and background. This is achieved by changing the water properties as well as the efficiency of the optical modules. The corresponding effect is of the order of 10% at the energies considered here.

Once these effects are taken into account, the observation can be translated into a 68% confidence interval and a 90% confidence level upper limit according to the method of [30] as reported in Figure 2 and Table 1. The energy ranges over which these results are valid is computed from Monte Carlo simulations, evaluating where the central 90% of signal events lies in the combined shower and track samples. The p-value of the observed excess is 0.15. It should be noted that, though not significant, the observation is fully compatible with the expectation from an IceCube-like cosmic contribution in addition to the atmospheric backgrounds. A more detailed analysis of the spectral behaviour of the observed excess is foreseen.

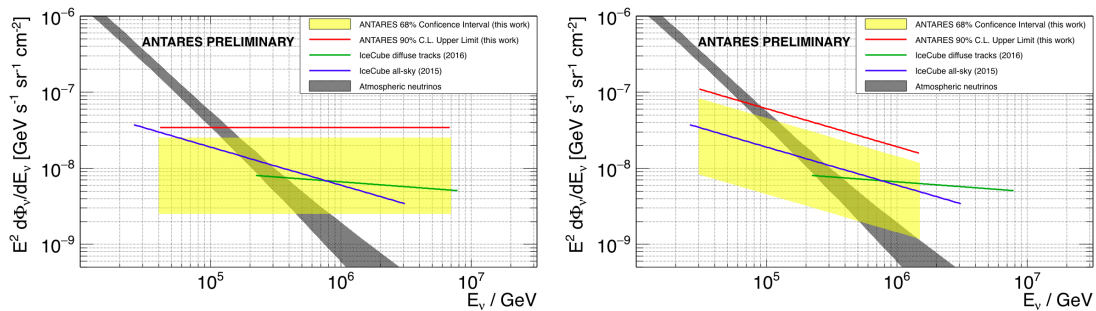


Figure 2: Upper limit at 90% C.L. (red line) and 68% confidence interval (yellow band) for the combined track and shower analysis, including systematics. These are compared to the atmospheric neutrino background (gray shaded area – including uncertainties as in the text) and the measurement from IceCube for the Northern sky with tracks (green line) [8] and the combined all-sky analysis (blue line) [7]. Left panel is for a signal spectrum proportional to  $E^{-2}$ , right for  $E^{-2.5}$ .

## References

- [1] S.R. Kelner, F.A. Aharonian and V.V. Bugayov, Phys. Rev. D **74** (3): 034018 (2006).
- [2] K. Mannheim, R. Protheroe and J.P. Rachen, Phys. Rev. D **63**: 023003 (2001).

- [3] E. Waxman and J. Bahcall, *Phys. Rev. D* **59**: 023002 (1998).
- [4] E. Fermi, *Phys. Rev.* **75**: 1169 (1949) and E. Fermi, *Astrophys. J.* **119**: 1 (1954).
- [5] A. Loeb and E. Waxman, *JCAP* **05**: 003 (2006).
- [6] M.G. Aartsen et al., *Phys. Rev. Lett.* **113**: 101101 (2014).
- [7] M.G. Aartsen, et al., *Astrophys. J.* **809**: 98 (2015).
- [8] M.G. Aartsen et al., *Astrophys. J.* **833** no.1: 3 (2016).
- [9] A. Palladino, M. Spurio and F. Vissani, *J. Cosmol. Astropart. Phys.* **16**(12): 045 (2016).
- [10] M. Ageron et al., *Nucl. Instrum. Meth. A* **656**: 11 (2011).
- [11] S. Adrián-Martínez et al., *Astrophys. J.* **786**: L5 (2014).
- [12] S. Adrián-Martínez et al., *Phys. Lett. B* **760**: 143 (2016).
- [13] J.A. Aguilar et al., *Phys. Lett. B* **696**: 16 (2011).
- [14] S. Biagi et al., *Proceedings of the 2013 Rencontres de Moriond* (2014).
- [15] J. Schnabel et al., *POS(ICRC2015)1065* (2015).
- [16] A. Albert et al., *Eur. Phys. Journ. C* **77**: 419 (2017).
- [17] A. Heijboer, *arXiv:0908.0816* (2008).
- [18] J. Schnabel et al., *Nucl. Instr. and Meth. A* **725**: 106-109 (2013).
- [19] T. Michael et al., *POS(ICRC2015)1078* (2015).
- [20] L.A. Fusco and A. Margiotta, *Proceedings of the VLVnT 2015 Conference, Rome* (2015).
- [21] Y. Becherini et al., *Astrop. Phys.* **25**: 1 (2006).
- [22] G. Carminati et al., *Comput. Phys. Commun.* **179**: 915-923 (2008).
- [23] M. Honda et al., *Phys. Rev. D* **75**: 043006 (2007).
- [24] R. Enberg et al., *Phys. Rev. D* **78**: 043005 (2008).
- [25] S. Adrián-Martínez et al., *Eur. Phys. Journ. C* **73**: 2606 (2013).
- [26] G.C. Hill and K. Rawlins, *Astrop. Phys.* **19**: 393 (2003).
- [27] G.J. Feldman and R.D. Cousins, *Phys. Rev. D* **57**: 3873-3889 (1998).
- [28] A. Albert et al., submitted to *Phys. Rev. D* (2017), *arXiv:1706.01857*.
- [29] T.K. Gaisser, T. Stanev, and S. Tilav, *arXiv:1303.3565* (2013).
- [30] J. Conrad et al., *Phys. Rev. D* **67**: 012002 (2003).

## Neutrinos from the Fermi Bubbles with ANTARES

---

### Steffen Hallmann\*

*Universität Erlangen-Nürnberg, Erwin-Rommel-Str. 1, 91058 Erlangen, Germany*

*Erlangen Centre for Astroparticle Physics (ECAP)*

*E-mail: [steffen.hallmann@fau.de](mailto:steffen.hallmann@fau.de)*

### Thomas Eberl

*Universität Erlangen-Nürnberg, Erwin-Rommel-Str. 1, 91058 Erlangen, Germany*

*Erlangen Centre for Astroparticle Physics (ECAP)*

*E-mail: [thomas.eberl@fau.de](mailto:thomas.eberl@fau.de)*

### on behalf of the ANTARES Collaboration

The Fermi Bubbles are giant lobe-shaped structures of  $\gamma$ -ray emission extending above and below the Galactic Center. A variety of both hadronic and leptonic models has been proposed to explain the emission, yet its origin remains unclear. Only in hadronic scenarios, the  $\gamma$ -ray flux is accompanied by an associated neutrino flux that might be detected with large volume neutrino detectors. ANTARES is the largest neutrino telescope in the Northern Hemisphere and has been operated in its final configuration since 2008. Its location in the Mediterranean sea provides an excellent view towards the Fermi Bubbles' region. In a previous analysis ANTARES has observed a non-significant excess of neutrinos in the Fermi Bubble region using charged current interactions of  $\nu_\mu$ . For these events, the outgoing muon produces an elongated track-like signature that can be reconstructed with sub-degree angular resolution. More recently, improved shower reconstruction algorithms achieve a precision of  $\sim 3^\circ$  also for signatures produced in  $\nu_e$ ,  $\nu_\tau$  and neutral current interactions. This contribution presents the search for shower-like events from the Fermi Bubbles in ANTARES data. In combination with the previous analysis, upper limits on the all-flavour neutrino emission from the region are derived.

*35th International Cosmic Ray Conference — ICRC2017*

*10–20 July, 2017*

*Bexco, Busan, Korea*

---

\*Speaker.

## 1. The Fermi Bubbles – giant lobes of $\gamma$ -rays and neutrinos?

The Fermi Bubbles are two giant areas of bright high-energy  $\gamma$ -ray emission extending  $50^\circ$  above and below the Galactic Center. Although the structure has been first observed in Fermi-LAT data in 2010 [1, 2], its origin is still not unambiguously identified. Most of the proposed emission scenarios suggest  $\gamma$ -ray generation by either leptons [3, 4, 5] or hadrons [6, 7, 8]. In hadronic scenarios, high energy protons, diffused from the environment of the Galactic Center, produce charged mesons and subsequently  $\gamma$ -rays upon interaction with the ambient gas. In this case the decays of (mainly) charged pions give rise to an accompanying neutrino flux that can be searched for with large-volume neutrino detectors like the ANTARES telescope. In case the origin is leptonic, the  $\gamma$ -ray flux from synchrotron emission of high energy  $e^\pm$  lacks a neutrino counterpart. Ultimately, (non-)observation of a neutrino flux from the Fermi Bubbles can therefore constrain the hadronic component of the  $\gamma$ -ray flux.

ANTARES [9] is a neutrino telescope located at the bottom of the Mediterranean Sea in a depth of 2.5 km. It consists of 885 optical modules (OMs) distributed over twelve detection lines that register Cherenkov radiation induced by charged secondary particles emerging from neutrino interactions in the sea water. In the detector, neutrinos can have two main event topologies. In charged-current (CC) interactions of high energy  $\nu_\mu$ , the produced muon travels several hundred meters in sea water while emitting Cherenkov light. The detected signature in the optical sensors appears therefore track-like. The second topology has a more contained emission – shower-like events – and is produced by CC interactions of  $\nu_e$  and neutral-currents of all flavours. The tau-lepton produced in CC interactions of  $\nu_\tau$  decays rapidly and mostly gives rise to shower-like signatures. Only in its decay to a muon (17%), the event may appear track-like.

Track signatures have already been analysed in a previous analysis [10] in the data recorded with ANTARES between May 2008 and December 2015. Here, we present the search for shower-like events in the same period and derive combined all-flavour upper limits on the Fermi Bubble neutrino flux.

## 2. Shape of the bubbles and analysis strategy

The measured  $\gamma$ -ray flux is to first order uniformly bright throughout the extension of the bubbles. When discovered, a hard spectrum close to  $\approx E^{-2}$  with no clear cutoff up to several hundred GeV was observed by Fermi-LAT [2]. With higher statistics and after more detailed analysis, either a sub-TeV cutoff or a significant softening at high energies is meanwhile preferred [11]. The shape of the Fermi Bubbles is shown in Fig. 1 (left). While a tentative flux-intense ‘cocoon’ shape in the central region has been suggested earlier on [11], it was only recently that the Fermi Bubbles have been analysed at latitudes below  $10^\circ$  [12]. Here, a relatively hard  $\sim E^{-2.1}$  with no cutoff up to several 100 GeV is observed. Also, the  $\gamma$ -ray flux in the low-latitude region is three times higher compared to the rest of the bubbles. This might be a hint of a change in the composition of the Fermi Bubbles towards low latitudes.

However, as the possible emission region of neutrinos is not known a priori, the same simplified hourglass shape as in the track analysis is used as signal region. The background in this on-zone

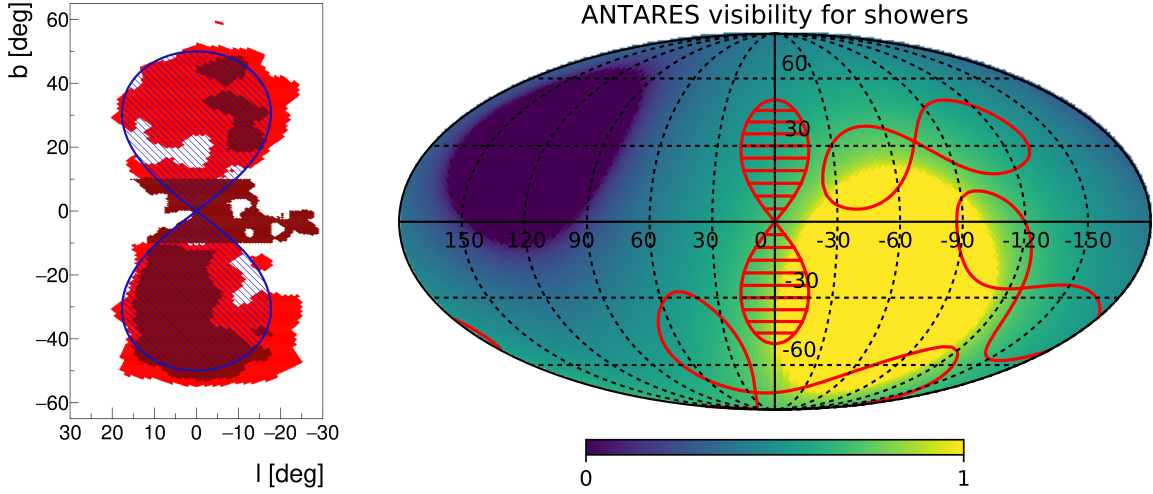


**Figure 1:** *Left:* Shapes of the Fermi Bubbles' templates observed at high and low latitudes by Fermi-LAT [11, 12]. The hourglass shape used in the analysis is indicated in blue. *Right:* On- and off-zones in Galactic coordinates. The color code shows the visibility for events in the shower analysis.

is estimated from three off-zones shifted in time by  $1/4$ ,  $1/2$  and  $3/4$  sidereal days to ensure similar visibility for each zone (see Fig. 1 (right)).

### 3. Assumed spectrum and flux

For the emission we assume a uniform  $\gamma$ -ray flux of

$$E^{2.18} \frac{d\Phi_\gamma}{dE} = (0.5 - 1.0) \times 10^{-6} \text{ GeV}^{1.18} \text{ cm}^{-2} \text{ s}^{-1} \text{ sr}^{-1} \quad (3.1)$$

throughout the signal shape, corresponding to an  $\sim E^{-2.25}$  proton flux [13]. Previously, ANTARES tested also a harder  $E^{-2}$   $\gamma$ -ray spectrum. However such a spectrum is meanwhile significantly constrained by the HAWC telescope unless for very low cutoff energies in the GeV domain [14]. As shown in Fig. 2, high cutoff energies are meanwhile disfavoured even for the softer spectrum.

For the softer spectral index, the corresponding neutrino (anti-neutrino) flux per flavour in a purely hadronic scenario is a factor 0.188 (0.175) smaller than the  $\gamma$ -ray emission given neutrino oscillation has equalised the flavour composition  $\nu_e : \nu_\mu : \nu_\tau = 1 : 1 : 1$  at the detector [15].

Within our galaxy sources are not expected to efficiently accelerate protons beyond  $1 - 10 \text{ PeV}$  in energy [6]. This induces also a cutoff in the observed  $\gamma$ -ray and neutrino spectra. As an approximation 20% of the proton energy is on average converted into charged pions. Equipartition of this energy over the four daughters in pion decay yields  $E_{\text{cutoff},\nu} = 0.05 \times E_{\text{cutoff},p}$  for neutrinos, i.e. optimistic cutoff energies ranging from 50 to 500 TeV.

Hence, the probed neutrino fluxes per flavour are:

$$E^{2.18} \frac{d\Phi_{\text{model}}}{dE} = (1.8 - 3.6) \times 10^{-7} \text{ GeV}^{1.18} \text{ cm}^{-2} \text{ s}^{-1} \text{ sr}^{-1} \times \exp\left(-\frac{E}{E_{\text{cutoff},\nu}}\right), \quad (3.2)$$

with  $E_{\text{cutoff},\nu} = [\infty, 500 \text{ TeV}, 100 \text{ TeV}, 50 \text{ TeV}]$ .



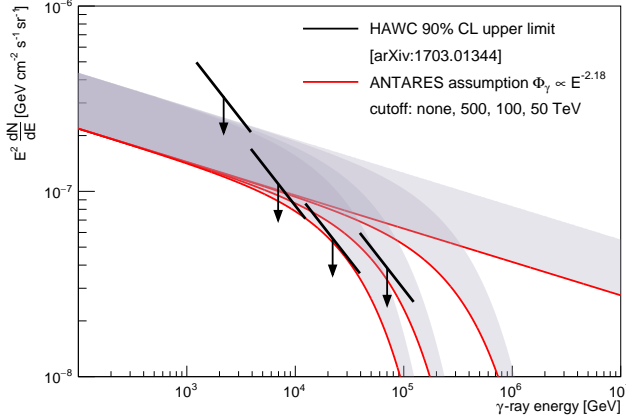


**Figure 2:** Assumed  $\gamma$ -ray flux bands (c.f. eq. 3.1) and HAWC upper limits [14] on the northern bubble. Conservative lower bounds (red lines) were used for the optimisation of the shower event selection. The same cutoff values as assumed for neutrinos are shown for illustration.

#### 4. Shower analysis: Event reconstruction and selection

For the shower analysis, all recorded runs with stable data-taking conditions are selected. In the period from March 2008 to December 2015 a total livetime of 2097 days is used.

Shower-like events in ANTARES are reconstructed with a recently developed algorithm [16] in two subsequent steps. First, the shower vertex is determined by minimising a robust M-estimator,  $M_{\text{est}}$ , using the charge and time of signal-like photon hits on the OMs. In a second step, the obtained vertex and the amplitudes registered by the OMs are used to perform a maximum likelihood fit of the shower direction and to estimate the neutrino energy,  $E_{\text{shower}}$ . With this algorithm a directional resolution of  $\lesssim 3^\circ$  is achieved for shower events.

Most of the reconstructed events in ANTARES are of atmospheric origin. Despite the overburden of sea water, muons produced in cosmic ray air showers can reach the detector from above. Therefore only event directions from below or close to the horizon,  $\cos(\text{zenith}_{\text{shower}}) < 0.1$ , are accepted. Since many mis-reconstructed atmospheric muons have a fitted vertex far outside the detector, events reconstructed close to the instrumented volume are selected, in particular the radial and vertical distance from the detector center are restricted to  $R_{\text{shower}} < 300$  m and  $|z_{\text{shower}}| < 250$  m, respectively. To reduce the contribution from atmospheric muons and badly reconstructed events in the analysis further, a series of additional selection cuts are applied. These are a cut on the  $M_{\text{est}}$  parameter, a cut on the shower likelihood ratio,  $L_{\text{shower}}$ , which uses information of the shower hits used in the fit, a cut on the angular error estimate  $\beta_{\text{shower}}$  of the shower reconstruction and cuts on two additional quality parameters from other algorithms. The latter two are the quality parameter of a grid-scan based track reconstruction algorithm,  $R_{\text{GridFit}}$ , and the output variable of a random decision forest (RDF) trained on the fit result of a second shower reconstruction algorithm [17]. In addition, only events that did not pass the final event selection of the track analysis [18, 10] are accepted to provide two disjoint event samples.

Atmospheric neutrinos may only be discriminated from a Fermi Bubble signal thanks to their soft  $\sim E^{-3.7}$  energy spectrum. As a consequence a lower cut on the energy estimate  $E_{\text{shower}}$  is applied. The full set of cuts is listed in Tab. 1.

Whilst some of the cuts serve only for a loose de-selection of badly reconstructed events, others are optimised by using the dedicated Monte Carlo simulation that is generated for each data-taking



**Table 1:** List of selection cuts for shower events. Further details on the parameters are given in the text. Cuts labeled with (\*) have been optimised to yield the optimal sensitivity for a neutrino cutoff at 50TeV. The others have been applied for pre-selection.

parameter	cut value		
$R_{\text{shower}}$	$< 300 \text{ m}$	...	
$ z_{\text{shower}} $	$< 250 \text{ m}$	$\cos(\text{zenith}_{\text{shower}})$	$< 0.1$ (*)
$M_{\text{est}}$	$< 1000$	$\beta_{\text{shower}}$	$< 30^\circ$ (*)
GridFit_R	$> 0.7$	$RDF$	$> 0.4$ (*)
does not pass track selection		$L_{\text{shower}}$	$> 20$ (*)
...		$E_{\text{shower}}$	$> 2290 \text{ GeV}$ (*)

run in ANTARES to account for the variable environmental conditions and the state of the detector. In the available Monte Carlo simulation, the  $\nu_\tau$  channel was not simulated on a run-by-run basis. The contribution of  $\nu_\tau$  was included by scaling the  $\nu_\mu$  CC and  $\nu_e$  CC and NC ratios adequately to take into account the  $\nu_\tau \rightarrow \mu$ ,  $\nu_\tau \rightarrow e$ ,  $\nu_\tau \rightarrow \text{hadron}$  contributions. [19]

The cuts on  $\cos(\text{zenith}_{\text{shower}})$ ,  $\beta_{\text{shower}}$ ,  $L_{\text{shower}}$ ,  $RDF$  and  $E_{\text{shower}}$  have been optimised to yield the most stringent average 90% upper limit on the Fermi Bubble flux,

$$\bar{\Phi}_{90\%} = \Phi_{\text{model}} \times \frac{\bar{s}_{90\%}(b)}{s}. \quad (4.1)$$

Here,  $s$  is the number of simulated and selected signal neutrinos generated and reconstructed within the signal region, and  $b$  is the average over simulated background events reconstructed within the off-zone regions. The average signal upper limit,

$$\bar{s}_{90\%}(b) = \sum_{k=0}^{\infty} \mu_{90\%}(k, b) \times \text{Poisson}(k|b), \quad (4.2)$$

is summed over Feldman-Cousins signal upper limits [20] with a 90% confidence level,  $\mu_{90\%}$ , for any possible event count in the on-zone,  $k$ , weighted with the respective Poisson probability. In the optimisation only the cut on the shower energy variable depends strongly on the assumed signal cutoff.  $E_{\text{shower}} > 2.29 \text{ TeV}$  is optimal for the 50TeV cutoff scenario and chosen as selection cut for the analysis. All other selection cuts applied are listed in Tab. 1. The number of background events per off-zone expected from Monte Carlo simulation is 8.9. Table 2 summarises the flux sensitivities and corresponding signal expectations for different cutoffs. The sensitivity in the shower channel alone is approximately an order of magnitude above the assumed flux. The sensitivity of ANTARES worsens significantly for even lower cutoff energies due to the dominant atmospheric neutrino flux at low energies.

## 5. Observed shower events

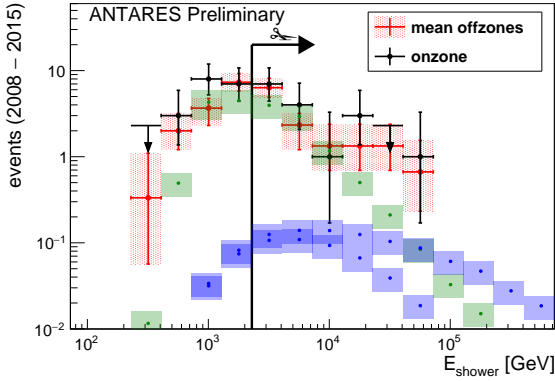
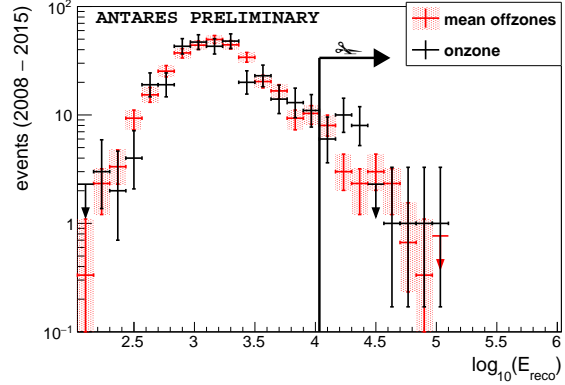
Good agreement of data and Monte Carlo simulation in the off-zones has been verified both with the loose pre-selection cuts and with the final selection excluding the cut on  $E_{\text{shower}}$  for all selection variables used. In addition, to ensure that the same number of events can be expected

**Table 2:** Flux sensitivities in units of the model flux per flavour and expected number of signal events for different cutoff values of the neutrino flux.

Cut-off energy	$\infty$	500 TeV	100 TeV	50 TeV
sensitivity / $\Phi_{\nu_\alpha + \bar{\nu}_\alpha}$	7.2	8.7	12	15
signal (Monte Carlo)	0.90	0.75	0.55	0.44

from all analysis zones, it has been checked using a variety of randomly chosen selection cut values that the simulated event counts agree on the percent level between on- and the average over the off-zones and that the off-zone difference of data events is within the expectation from statistical fluctuations.

Applying the event selection described above, a total of 40 events are observed in the three off-zones, resulting in an expected background of 13.3 events for the signal region. Here, 16 events are detected. This corresponds to a small and non-significant excess of  $0.6\sigma$  in the shower channel alone using the method from Ref. [21]. The  $E_{\text{shower}}$  distribution of the events in the on- and off-zones is presented in Fig. 3. Observed event counts in the zones slightly exceed the Monte Carlo expectation indicated as green band. To account for flux uncertainties, an additional 30% error on the neutrino flux is included in the error bands. In the selected event sample the statistics of simulated atmospheric muons is very low, which might explain the small excess of events seen in data with respect to the simulations. For the measurement however, the background is determined from off-zones without use of Monte Carlo simulations. Here, the event distribution in the on-zone is in good agreement with the off-zones.

**Figure 3:** Energy distribution of data (including  $1\sigma$  Poisson intervals) in the shower analysis with the event selection applied. The sum of the simulated Monte Carlo expectation from atmospheric and the possible Fermi Bubble flux with 50 TeV cutoff and no cutoff are shown as green and blue bands, respectively. The cut on the energy estimate  $E_{\text{shower}} > 2.29$  TeV is indicated.**Figure 4:** Energy distribution for data from the on- and off-zones in the track analysis (including  $1\sigma$  Poisson intervals) after event selection. The lower cut on the energy estimate  $E_{\text{reco}} > 10^{4.03}$  GeV is indicated. [10]

## 6. Summary of the track reconstruction and results

The previous analysis of the track channel in Ref.[10] analysed the same period from May 2008 to end 2015. Also in the track channel, a non-significant ( $1.5\sigma$ ) excess of 28 events was observed compared to an average number of 19.7 events seen inside the off-zones. Figure 4 shows the event distribution in the track channel. The visibility for the Fermi Bubbles in the track analysis is slightly reduced compared to showers, due to a zenith angle cut exactly at the horizon which is needed to limit the contribution from mis-reconstructed atmospheric muons.

## 7. All-flavour upper limits

The small over-fluctuations in the shower and the track analysis are non-significant. Therefore the on- and offzone counts of the track and shower analyses ( $N_{\text{on,t/s}}, \bar{N}_{\text{off,t/s}}$ ) are used to derive combined 90% upper limits on the Fermi Bubble neutrino flux:

$$\Phi_{90\%} = \Phi_{\text{model}} \times \frac{\mu_{90\%} (N_{\text{on,t}} + N_{\text{on,s}} | \bar{N}_{\text{off,t}} + \bar{N}_{\text{off,s}})}{s_t + s_s}. \quad (7.1)$$

Resulting upper limits are put in the region where the central 90% of the possible signal from the track and shower channel ( $s_t/s_s$ ) overlap in Fig. 5. Note that a detailed study of systematic uncertainties is ongoing and not yet included in the presented upper bounds. The bounds do not reach the sensitivity of ANTARES (cf. Tab. 2) due to the small excesses seen in both channels. The combined upper limits are a factor 0.72 (no cutoff) to 0.61 (50 TeV cutoff) more stringent than the upper limits obtained from the track analysis alone.

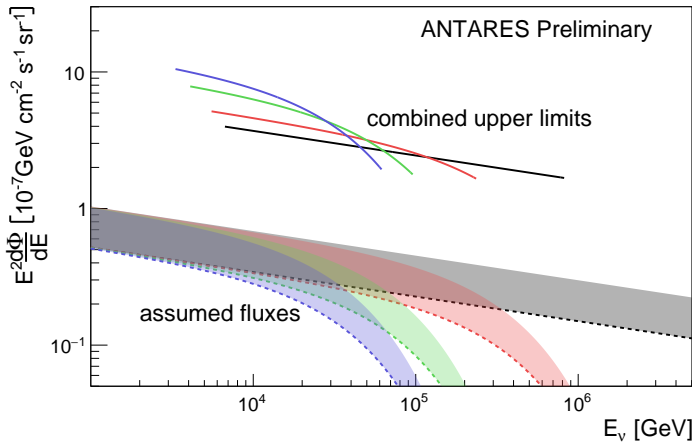


**Figure 5:** Combined 90% upper limits on the neutrino flux from the Fermi Bubbles for 50 TeV, 100 TeV, 500 TeV and no cutoff. Upper limits are restricted to the regions where the central 90% of signal from the track and shower channel overlap.

## 8. Conclusion

With the recent upper limits on the high energy photon flux from the Fermi Bubbles, optimistic assumptions for the neutrino flux to which ANTARES is most sensitive are disfavoured. The derived combined upper limits are an order of magnitude above the tested flux with a softer spectral index. Also, no evidence for a neutrino excess from the Fermi Bubbles region is observed in IceCube data [22, 23]. In future, the KM3NeT detector under construction in the Mediterranean

Sea will improve the event statistics and the sensitivity in the region of the bubbles [24]. Especially an extension to very high energies of the recently identified hard flux component at low latitudes [12] – which unfortunately is outside the field of view of the HAWC observatory – can be probed with neutrinos using the KM3NeT detector.

## References

- [1] G. Dobler, D. P. Finkbeiner, I. Cholis, T. Slatyer, and N. Weiner *ApJ* **717** (July, 2010) 825–842, [[arXiv:0910.4583](#)].
- [2] M. Su, T. Slatyer, and D. Finkbeiner *ApJ* **724** (2010) 1044, [[arXiv:1005.5480](#)].
- [3] P. Mertsch and S. Sarkar *Phys. Rev. Lett.* **107** (2011) 091101, [[arXiv:1104.3585](#)].
- [4] G. Dobler, I. Cholis, and N. Weiner *ApJ* **741** (2011) 25, [[arXiv:1102.5095](#)].
- [5] H.-Y. K. Yang and M. Ruzskowski *ArXiv e-prints* (June, 2017) [[arXiv:1706.0502](#)].
- [6] R. Crocker and F. Aharonian *Phys. Rev. Lett.* **106** (2011) 101102, [[arXiv:1008.2658](#)].
- [7] S. Thoudam *ApJ, Letters* **778** (2013) L20, [[arXiv:1304.6972](#)].
- [8] B. C. Lacki *Monthly Notices of the RAS* **444** (2014) L39, [[arXiv:1304.6137](#)].
- [9] M. Ageron and et al. *NIM A* **656** (Nov., 2011) 11–38, [[arXiv:1104.1607](#)].
- [10] T. Eberl and S. Hallmann for the ANTARES Coll. *Proceedings of the Neutrino 2016* (2016).
- [11] M. Ackermann et al. *ApJ* **793** (2014) 64, [[arXiv:1407.7905](#)].
- [12] The Fermi-LAT Collaboration *ArXiv e-prints* (Apr., 2017) [[arXiv:1704.0391](#)].
- [13] S. R. Kelner, F. A. Aharonian, and V. V. Bugayov *Phys. Rev. D* **74** (2006), no. 3 034018.
- [14] A. U. Abeysekara et al. *ApJ* **842** (2017) 2, 85.
- [15] F. L. Villante and F. Vissani *Phys. Rev. D* **78** (2008) 103007, [[arXiv:0807.4151](#)].
- [16] T. Michael, ANTARES Coll. *Proceedings of the 34th ICRC PoS (ICRC2015)* **1078** (2015).
- [17] ANTARES Collaboration *ArXiv e-prints* (Mar., 2017) [[arXiv:1703.0243](#)].
- [18] S. Adrian-Martinez et al. *Eur. Phys. J. C* **74** (2014) 2701, [[arXiv:1308.5260](#)].
- [19] ANTARES Collaboration *ArXiv e-prints* (2017) [[arXiv:1706.0185](#)].
- [20] G. J. Feldman and R. D. Cousins *Phys. Rev. D* **57** (1998) 3873, [[physics/9711021](#)].
- [21] T.-P. Li and Y.-Q. Ma *ApJ* **272** (1983) 317.
- [22] K. Fang, M. Su, T. Linden, and K. Murase *ArXiv e-prints* (2017) [[arXiv:1704.0386](#)].
- [23] N. Sherf, U. Keshet, and I. Gurwich *ArXiv e-prints* (2017) [[arXiv:1705.0666](#)].
- [24] KM3NeT Collaboration, S. Adrian-Martinez et al. *ApJ* **42** (2013) 7.

## Search for signal emission from unresolved point sources with the ANTARES neutrino telescope

---

**Rodrigo G. Ruiz**

*IPHC Strasbourg*

*E-mail: [rodrigo.gracia-ruiz@iphc.cnrs.fr](mailto:rodrigo.gracia-ruiz@iphc.cnrs.fr)*

**Bruny Baret**

*APC Paris*

*E-mail: [baret@in2p3.fr](mailto:baret@in2p3.fr)*

**Antoine Kouchner**

*APC Paris*

*E-mail: [kouchner@apc.univ-paris7.fr](mailto:kouchner@apc.univ-paris7.fr)*

### On behalf of the ANTARES collaboration

We use an autocorrelation analysis to look for inhomogeneities in the arrival directions of the high energy muon neutrino candidates detected by the ANTARES neutrino telescope. This approach is complementary to a point source likelihood-based search, which is mainly sensitive to one bright point like source and not to collective effects. We present the results of a search based on this two-point correlation method, providing constraints on models of a population of Active Galactic Nuclei (AGN) too faint to be detected by the likelihood-based method.

## 1. Introduction

The origin of cosmic rays (CR) is still an open question and major efforts are ongoing to identify the CR sources and the physical mechanisms by which the CR are accelerated up to energies of the order of  $\sim 10^{20}$  eV. The magnetic fields in the galactic and intergalactic space deflect the CRs during their propagation, making it difficult to derive the position of the sources from the CR arrival direction. The interactions of accelerated CR with radiation fields present in their acceleration sources lead to the production of neutrinos and gamma rays via the decay of charged and neutral pions. Unlike CR, gamma rays and neutrinos are electrically neutral and they point back to their sources. However, gamma rays cannot be used to unambiguously identify CR sources, since they can also be produced in the absence of accelerated hadrons (for instance, by synchrotron emission by accelerated electrons). In addition, gamma rays produced in dense regions cannot be directly observed because they get absorbed and reprocessed to lower energies. On the other hand neutrinos can only be produced in the presence of accelerated protons, and their low interaction cross section allows them to escape from dense regions. Therefore, neutrinos constitute a unique messenger which allows to unambiguously identify CR sources and to probe astrophysical environments that are not accessible with other messengers.

Theoretical arguments strongly suggest that Active Galactic Nuclei (AGN) are potential CR accelerators, and therefore sources of high energy neutrinos. Indeed, high energy neutrino emission from AGN jets has been the subject of theoretical discussions, and experimental analyses carried out by neutrino telescopes such as ANTARES and IceCube. In this contribution we present a new experimental analysis where we use the ANTARES neutrino telescope together with AGN luminosity functions inferred from the observations performed by Swift in the X-ray band. We evaluate the discovery power of the ANTARES telescope to populations of AGN that follow those luminosity functions, and constrain the neutrino emission from these objects in terms of two quantities: the fraction of X-ray emitting AGN that are also neutrino emitters, and the neutrino luminosity expressed as a fraction of the X-ray luminosity.

The ANTARES telescope aims to detect the Cherenkov light caused by charged leptons resulting from the interaction of cosmic neutrinos with the matter in and around the instrumented volume. The interaction of high energy cosmic rays with the Earth's atmosphere induces air showers in which among other particles, muons and neutrinos are present. These so called atmospheric muons and atmospheric neutrinos constitute the two main sources of background for the ANTARES detector. The Earth is opaque to all particles with the exception of neutrinos, because they interact only weakly with matter. Thus the atmospheric muon background can be reduced by selecting only those events that are reconstructed with an upwards direction with respect to the ANTARES neutrino telescope. Nevertheless, some muon tracks coming from above can be reconstructed as upward going. The amount of wrongly reconstructed muons can be reduced by means of quality cuts in the muon tracks reconstruction parameters. On the other hand, atmospheric neutrinos remain as an irreducible source of background. Its good angular resolution (better than 0.4 for energies above 10 TeV) for muon tracks allows ANTARES for the search of small scale anisotropies within the isotropic background produced by atmospheric events. One way of doing this is by means of an autocorrelation analysis, which is well suited for the search of anisotropies produced by the collective effect of an ensemble of point-like sources, such as the AGN populations that we

want to study.

This work is organised as follows. In section 2 the analysis method using an autocorrelation function is explained, and the data set used for this analysis is presented. In section 3, details on the simulation of AGN populations are given and the discovery power of the autocorrelation analysis is tested with those populations. Finally, the results after applying the autocorrelation analysis to the ANTARES data set are shown in section 4. Since we didn't find any significant excess with respect to the background only expectation, upper limits on the AGN populations are also shown.

## 2. Analysis method and data set

We use the autocorrelation analysis, which allows to find inhomogeneities within a discrete data set by studying the autocorrelation distribution. This is defined as the distribution of the number of pairs of events as a function of their mutual angular distance  $\Delta\Omega$ . A comparison of the autocorrelation distribution resulting from the observed events with the one representing pure background samples, allows to detect possible clusters if a significant excess with respect to the pure background is present in the data. In this work we apply this method based on the description given in references [2] and [4].

For the present analysis, a data set recorded by the ANTARES neutrino telescope between 2007 and 2012 has been used. The sample contains 5243 neutrino candidates that have been selected using criteria optimized to obtain the best average upper limit on the flux of neutrinos coming from point like sources. These selection criteria consist in a cut on the reconstructed zenith angle  $\theta > 90^\circ$ , a cut on the angular uncertainty in the track reconstruction  $\beta < 1^\circ$ , and a cut on the reconstruction quality parameter  $\Lambda > -5.2$ . A cut is also applied on the  $N_{hit}$  energy estimator, which is defined as the number of Optical Modules (OMs) used in the reconstruction of a track. The cut  $N_{hit} > 50$  has been applied. After applying this cut, a total of 1555 events remain in the sample.

## 3. Autocorrelation analysis and populations of AGN

In this work, we use the autocorrelation analysis to constrain the neutrino emission from populations of AGN. We model AGN populations by defining two parameters. One related to the possible number of AGN that are neutrino emitters, and another related to the mean number of neutrinos that are reconstructed by the ANTARES telescope for each AGN.

### 3.1 Number of neutrino-emitter AGN

Observations across the electromagnetic spectrum have allowed to infer information on the abundance of AGN and to build phenomenological models that describe the astrophysical processes within. For instance, observations in the X-ray band by the Swift and Chandra satellites, have allowed to estimate the distribution of X-ray emitting AGN in the Universe. Such distribution is given by the so-called X-ray Luminosity Function (XLF), which is defined as

$$\text{XLF} \equiv \frac{d^2N}{dL_X dz} \quad (3.1)$$

where  $L_X$  is the amount of energy emitted per unit time in the X-ray band, and  $z$  is the redshift. Here we use the results from [6], where the XLF is computed for four different AGN classes (BL



Lac, FSRQ, Blazars and Radio Galaxies) in the ranges  $0 < z < 10$  and  $10^{44} \text{erg/s} < L_X < 10^{48} \text{erg/s}$ . A graphical representation of the XLF for Blazars is shown in figure 1 left. The total number of AGN emitting in X-rays in the considered  $(L_X, z)$  range  $N_X$ , can be found by integrating the XLF over all the phase space.

In this work we have considered that a fraction of the AGN that are X-ray emitters are also neutrino emitters,  $N_V = \eta \cdot N_X$ , where  $\eta$  is left as a free parameter that allows to explore populations with different numbers of AGN.

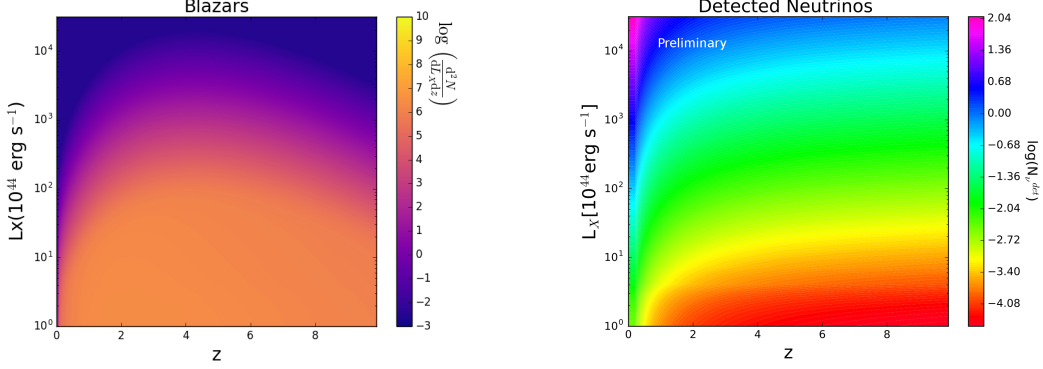


Figure 1: Left: The XLF for Blazars as defined by equation 3.1, as a function of the X-ray luminosity  $L_X$  and redshift  $z$ . Right: Number of neutrinos that ANTARES would detect from an AGN assuming  $L_X = L_V$ , as a function of  $z$  and  $L_X$ .

### 3.2 Neutrinos from AGN in ANTARES

Here we assume that the sources emit neutrinos with a spectral energy distribution given by an  $E^{-2}$  power law. In that case the neutrino flux at the Earth can be written as  $\phi_V = \phi_0 \cdot E^{-2}$ , where  $\phi_0$  is called the normalization flux of the source at the Earth and has units of  $(\text{GeV} \cdot \text{cm}^{-2} \cdot \text{s}^{-1})$ . The number of detected neutrinos that a source is expected to produce in ANTARES can be found through its acceptance  $A_\delta$  as a function of the declination  $\delta$ , as

$$N_V^{\text{det}} = \phi_0 \cdot A_\delta \quad (3.2)$$

where  $A_\delta$  has units of  $(\text{GeV}^{-1} \cdot \text{cm}^2 \cdot \text{s})$ .  $N_V^{\text{det}}$  can be computed as a function of the intrinsic properties of a source by relating  $\phi_0$  with the source luminosity. For an AGN at a luminosity distance  $d_L(z)$  from the Earth and characterized by a neutrino luminosity  $L_V$ , the amount of energy arriving at the Earth per unit time can be written as  $\varepsilon = L_V / (4\pi d_L^2(z))$ . If the source emits neutrinos with an  $\sim E^{-2}$  spectrum,  $\varepsilon$  can be rewritten as

$$\frac{L_V}{4\pi d_L^2(z)} = \int_{E_{\min}}^{E_{\max}} E \phi_V dE = \int_{E_{\min}}^{E_{\max}} E \phi_0 E^{-2} dE = \phi_0 \log \left( \frac{E_{\max}}{E_{\min}} \right) \quad (3.3)$$

Assuming that the neutrino luminosity relates to the X-ray luminosity by a proportionality constant as  $L_V = k \cdot L_X$ , the expected average of the number of detected events for a source at redshift  $z$  and with X-ray luminosity  $L_X$  can be written as

$$N_V^{\text{det}}(L_X, z) = \frac{kL_X}{4\pi r_L^2(z)} \langle A \rangle \left[ \log \left( \frac{E_{\max}}{E_{\min}} \right) \right]^{-1} \quad (3.4)$$



where  $\langle A \rangle$  is the acceptance averaged over all the declinations and integrated over the energy range  $1\text{GeV} < E < 1\text{PeV}$ . Figure 1 right shows  $N_\nu^{\text{det}}$  in the  $(z, L_X)$  plane for  $k = 1$ .

In order to simulate populations where the amount of neutrinos detected from each source remains consistent with the XLF, the results from section 3.1 and equation 3.4 can be used to build a pdf for the mean number of detected neutrinos for each AGN class which depends on the parameter  $k$ . This is done by dividing the phase space  $(L_X, z)$  into a high number of bins (in this case,  $\sim 10^4$ ). The total number of AGN in the bin  $ij$  can be found as  $(N_{\text{AGN}})_{ij} = \int_{ij} XLF dL_X dz$ , and the mean number of detected neutrinos as  $\langle N_\nu^{\text{det}} \rangle_{ij} \approx \frac{1}{\Delta L_X \Delta z} \int_{ij} N_\nu^{\text{det}} dL_X dz$ <sup>1</sup>. Figure 2 shows for different values of  $k$ , a pdf obtained by histogramming the quantity  $\langle N_\nu^{\text{det}} \rangle_{ij}$  weighted by  $(N_{\text{AGN}})_{ij}$  and normalising the resulting distribution to 1. These distributions are used to generate the signal neutrinos for each AGN in the population as explained in section 3.3

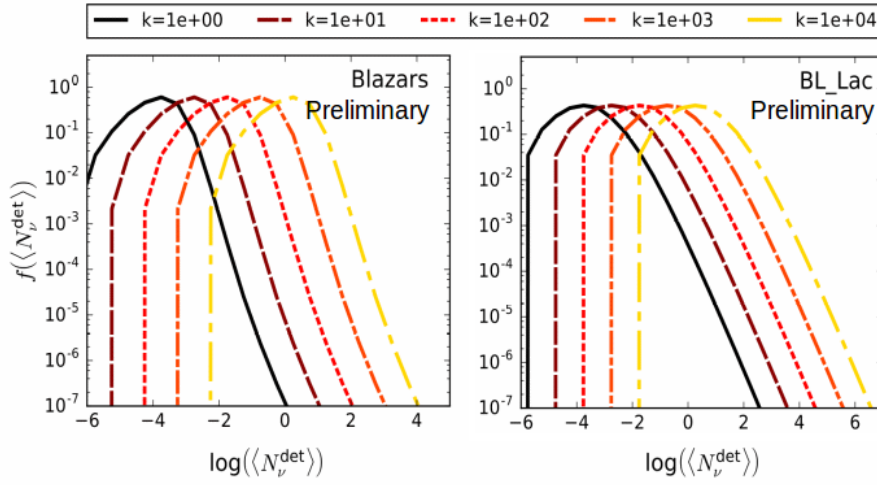


Figure 2: Probability distributions of the mean number of detected neutrinos for the different AGN families, and for different values of the parameter  $k$ .

### 3.3 AGN populations in ANTARES

The imprints that an AGN population characterized by the parameters  $(\eta, k)$  would leave in the ANTARES telescope are simulated as follows:

1. A number of sources  $N_S$  is determined by the choice of  $\eta$ , as a fraction of the total number of AGN that are X-ray emitters in the considered range of  $L_X$  and  $z$ .
2. A pure background data set  $\mathcal{S}_{\text{bg}}$  is generated as described in section 2.
3. For each source in the population,
  - (a) The source location is generated from flat distributions in right ascension and declination.

<sup>1</sup>This expression is valid as long as the bin size is small enough to consider that the XLF is constant

- (b)  $\langle N_v^{\text{det}} \rangle$  is sampled from the distribution as the ones shown in figure 2, corresponding to the choice of  $k$ .
  - (c) For each source,  $N_v^{\text{det}}$  is sampled from a Poisson distribution  $P(\langle N_v^{\text{det}} \rangle \cdot (\omega_v))$ , where  $\omega_v$  is a weight based on the ANTARES visibility, which depends on the source declination.
  - (d) The position of each neutrino in the source is generated from a 2D Gaussian distribution centred in the source's coordinates
4. As a result from the previous steps, a collection of coordinates of the signal neutrinos is obtained,  $\{(\alpha, \delta)_v\}$ . For each of the signal neutrinos, a neutrino in  $\mathcal{S}_{\text{bg}}$  is removed from its position and reallocated in the signal neutrino's coordinates.

### 3.4 Discovery power of the autocorrelation analysis for AGN populations

The discovery power of the autocorrelation analysis has been computed for populations of AGN characterised by several values of the parameters  $\eta$  and  $k$ . The choice of the  $(\eta, k)$  phase space is done so that the following conditions are satisfied:

- There are no more AGN emitting neutrinos than AGN emitting X-rays.
- There is at least an AGN emitting X-rays that also emits neutrinos.
- As it was shown in [2], the autocorrelation method is less sensitive to a single point source than a likelihood based search. Since we are interested on sources that cannot be detected by the latter method, we require the sources in the population to be weak neutrino emitters.
- A sample of events containing signal from an AGN population should be background dominated. To be consistent with the uncertainties on the atmospheric background [5], AGN populations where the amount of signal exceeds 30% of the total sample are not analysed.

The first two conditions constrain the range of the parameter  $\eta$ , which is related to the number of sources in the population. On the other hand, the parameter  $k$  controls the mean number of signal events produced by each source, and is constrained by the two last conditions. For those couples  $(\eta, k)$  that satisfy the previous conditions, the discovery power is computed as the probability that a population produces a  $3\sigma$  excess over the background. For each couple  $(\eta, k)$ , this is done by finding the corresponding distribution of the test statistic  $\lambda$ , and comparing it to that for pure background sets. The results are shown in figure 3.1.

## 4. Unblinding results, and limits to AGN populations

After performing the autocorrelation analysis with the unblinded set of events introduced in section 2, a p-value of 0.49 is found which is not statistically significant to reject the background only hypothesis. When the analysis of the observed data does not produce a statistically significant result, the observed value of the test  $\lambda_{\text{obs}}$  can be used to exclude the existence of models of sources of signal. For the AGN populations, all the combinations  $(\eta, k)$  for which a value of the test higher than  $\lambda_{\text{obs}}$  would be observed in at least a 90% of the cases, are said to be excluded with a 90%

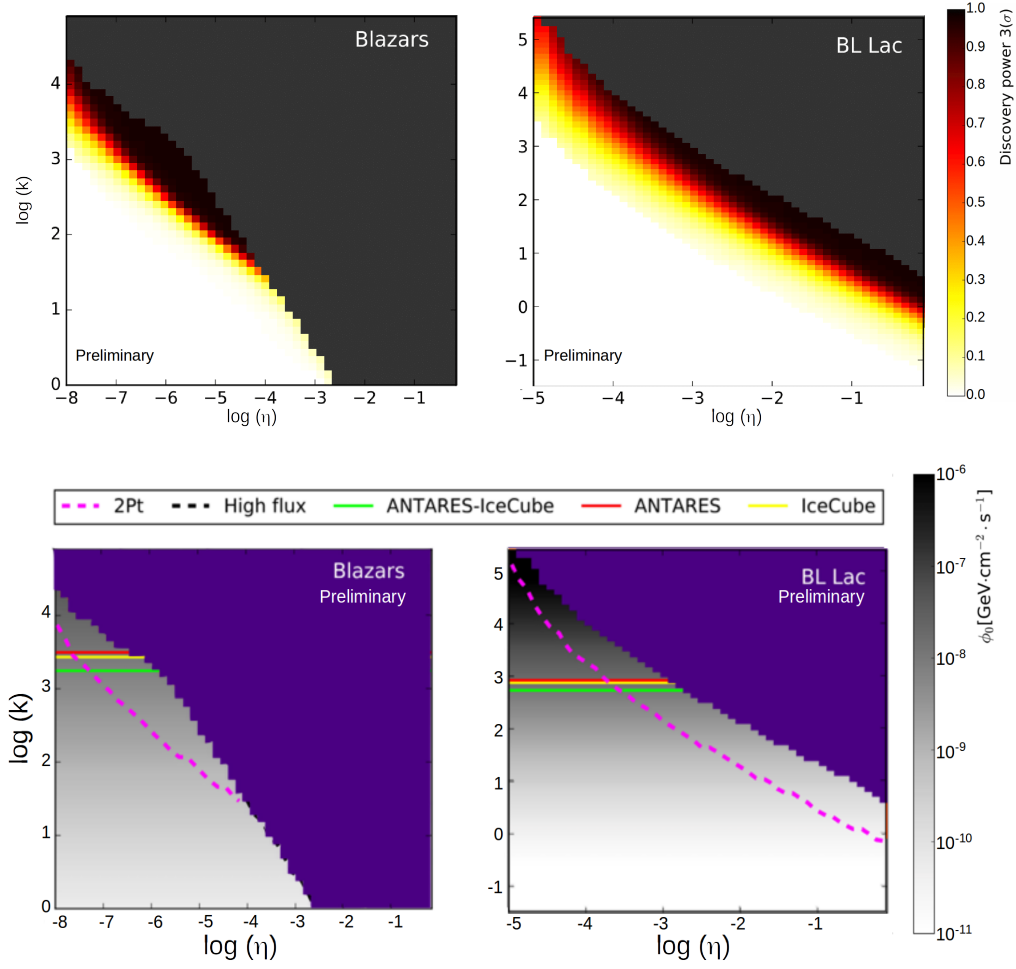


Figure 3: Top: Discovery power for blazars and radio galaxies as a function of the parameters  $\eta$  and  $k$ . Bottom: Limits on the  $(\eta, k)$  plane set by ANTARES for blazars and radio galaxies. The horizontal lines show the median upper limits from regular point source searches. Similar results were obtained for BL Lac and FSRQ.

confidence level. The values of  $\eta$  and  $k$  which are excluded by the autocorrelation analysis are shown in figure 3 bottom.

The color scale corresponds to the average flux per source. Additionally, upper limits on the neutrino flux from a point source are shown for IceCube (yellow), ANTARES (red) and a combined analysis using both data sets (green) are shown. These values have been extracted from reference [7], where a search for point sources is performed with the ANTARES and IceCube data sets separately, and with a combination of both. The search method consists on finding the most significant cluster in a given sky region, and the search was performed for different declination values in the range  $-1.0 < \sin(\delta) < 0$ . The corresponding lines in figure 3 show the median values over all the declinations for each of the data sets for an  $E^{-2}$  energy spectrum. The comparison of these limits with the limits calculated here with the autocorrelation analysis, confirms some of the results shown in reference [2], where it is shown that the likelihood based search is more

sensitive to a single point source than the autocorrelation analysis. This is reflected in the limits for the lowest values of the parameter  $\eta$ , which are less stringent for the autocorrelation analysis. In addition, this plot also shows that the autocorrelation analysis provides with much better limits for a point source flux, when populations of weak point sources are considered.

## 5. Conclusions

The autocorrelation analysis has been presented. Since this method is able to detect an excess of anisotropies produced by sources of different morphologies, it has been used to search for neutrinos produced by populations of different classes of AGN. These populations, which have been modelled from X-ray observations are characterized by two parameters  $\eta$  and  $k$ , which respectively represent the amount of X-ray emitting AGN that also emit neutrinos, and the fraction proportion between the neutrino and X-ray luminosity of the sources. The absence of a statistically significant departure from background in the ANTARES 2007-2012 data set has allowed to constrain the space defined by  $\eta$  and  $k$  for each AGN class.

## References

- [1] J.A. Aguilar et al. *ANTARES: the first undersea neutrino telescope*, Nuclear Inst. and Methods in Physics Research, A 656 (2011) pp. 11-38
- [2] S. Adrián-Martínez et al. *Searches for clustering in the time integrated skymap of the ANTARES neutrino telescope*, JCAP05 (2014)0001
- [3] S. Adrián-Martínez et al. *Search for cosmic neutrino point sources with four year data of the ANTARES telescope*, The Astrophysical Journal 760:53(2012)
- [4] F. Schuessler on behalf of the ANTARES Collaboration in the 2013 ICRC proceedings, *2pt correlation analysis of ANTARES data*, arXiv:1312.4308 [astro-ph.HE].
- [5] Agrawal et al. *Atmospheric neutrino flux above 1-GeV*, Phys. Rev. D 53, 1314-1323
- [6] I. Jacobsen et al. *High-energy neutrino fluxes from AGN populations inferred from X-ray surveys*. MNRAS, 451(4): 3649 - 3663 2015.
- [7] S. Adrián-Martínez et al. *First combined search for neutrino point-sources in the Southern Hemisphere with the ANTARES and IceCube neutrino telescopes*, The Astrophysical Journal 823 (2016) 65

# All-flavor Neutrino Point-like Source Search with the ANTARES Neutrino Telescope

## J. Barrios

IFIC - Instituto de Física Corpuscular (CSIC - Universitat de València) c/ Catedrático José Beltrán, 2 E-46980 Paterna, Valencia, Spain

E-mail: [javier.barrios@ific.uv.es](mailto:javier.barrios@ific.uv.es)

## G. Illuminati\*

IFIC - Instituto de Física Corpuscular (CSIC - Universitat de València) c/ Catedrático José Beltrán, 2 E-46980 Paterna, Valencia, Spain

E-mail: [giulia.illuminati@ific.uv.es](mailto:giulia.illuminati@ific.uv.es)

## on behalf of the ANTARES Collaboration

A search for cosmic neutrino sources using the data collected with the ANTARES detector between early 2007 and the end of 2015 is presented. For the first time, all neutrino interactions are considered in a search for point-like sources, instead of only muon neutrino charged current interactions. This is achieved by using a novel reconstruction algorithm for shower-like events in addition to the standard muon track reconstruction. In order to find the clusters of neutrinos from point-like sources over the randomly distributed atmospheric neutrino events, a maximum likelihood ratio approach is followed. The search for astrophysical neutrino sources is performed with four strategies. In the full-sky search, the whole visible sky of ANTARES is scanned to find the most significant cluster of events. In the second approach, the directions of a pre-defined list of known sources which are potential neutrino emitters are investigated. The third search is similar to the full-sky search but restricted to a region around the Galactic Center (GC). Finally, the fourth approach tests the location of Sagittarius A\* as an extended source by assuming a Gaussian emission profile of various widths. No significant evidence of cosmic neutrino sources is found. The most significant cluster in the full-sky search is located at  $(\alpha, \delta) = (343.8^\circ, 23.5^\circ)$  with a post-trial significance of  $1.9\sigma$ . Upper limits on the total neutrino flux from the investigated astrophysical candidates are set between  $0.60 \times 10^{-8}$  and  $2.1 \times 10^{-8}$   $\text{GeV cm}^2 \text{s}^{-1}$ . These searches provide the most sensitive limits for a large fraction of the Southern Sky, especially at neutrino energies below 100 TeV.

35th International Cosmic Ray Conference – ICRC217-  
10-20 July, 2017  
Bexco, Busan, Korea

---

\*Speaker.

## 1. Introduction

In these proceedings, the results of the latest searches for point-like sources using the ANTARES neutrino telescope [1] are presented. In this work also events identified as electromagnetic or hadronic showers are included in the search for point-like source, unlike previous analyses where only the information from track-like events was exploited. Shower-like events, which contribute about 23 % of all accepted  $E^{-2}$  signal events, are reconstructed by means of a new reconstruction algorithm [2], which achieves a median angular resolution between  $2^\circ$  and  $3^\circ$  for neutrinos with energies in the  $10^3 - 10^6$  GeV range.

## 2. Data Sample

In this analysis, data recorded from Jan 29, 2007 to Dec 31, 2015 are used, for a total livetime of 2423.6 days. The selection of events is performed according to a blinding policy, i.e. using real data scrambled in right ascension (PEs or pseudo-experiments). The selection cuts are chosen so that the neutrino flux needed to make a  $5\sigma$  discovery in 50% of the pseudo-experiments is minimised when assuming an  $E^{-2}$  spectrum. A summary of the different selection criteria for tracks and showers is given below. For the full list of selection cuts, refer to [3].

*Muon Track Selection.* The muon sample is optimised using three parameters provided by the track reconstruction algorithm – a multi-step fitting procedure that estimates the direction and the position of the muon by means of a maximum likelihood method [4]. Cuts are applied on the reconstructed zenith angle ( $\cos \theta_{tr} > -0.1$ ), the estimated angular error ( $\beta_{tr} < 1^\circ$ ) and the parameter that describes the quality of the reconstruction ( $\Lambda > -5.2$ ). An approximation of the muon energy deposit per unit path length is employed as a proxy of the muon energy [5, 6]. Two additional cuts on energy-related variables are applied to ensure the validity of the energy estimator. The selection yields a total of 7629 neutrino candidates in the track channel.

*Shower Selection.* Only events not passing the muon track selection are considered in the shower channel. The selection requires that the shower events are reconstructed as up-going or coming from close to the horizon ( $\cos \theta_{sh} > -0.1$ ) with constraints on the angular error estimate ( $\beta_{sh} < 30^\circ$ ) and on the interaction vertex, which is required to be reconstructed inside or close to the instrumented volume. The remaining background from mis-reconstructed atmospheric muons is further reduced applying additional selection cuts based on parameters provided by two different shower reconstruction algorithms. A total of 180 neutrino candidates are selected in the shower channel.

## 3. Search Method

A maximum likelihood estimation is performed to identify clusters of cosmic neutrinos from point-like sources over the background of randomly distributed atmospheric neutrinos. The likelihood, by means of signal and background probability density functions (PDFs), exploits the information from different parameters that help to distinguish signal-like clusters from clusters produced by random agglomerations of background events. The used likelihood is defined as

$$\log \mathcal{L}_{s+b} = \sum_S \sum_{i \in S} \log \left[ \mu_{\text{sig}}^S \mathcal{F}_i^S \mathcal{P}_{\text{sig},i}^S + \mathcal{N}^S \mathcal{B}_i^S \mathcal{P}_{\text{bkg},i}^S \right] - \mu_{\text{sig}}. \quad (3.1)$$

In this equation,  $S$  denotes the sample (*tr* for tracks, *sh* for showers),  $i$  indicates the event of the sample  $S$ ,  $\mu_{\text{sig}}^S$  is the number of signal events fitted for in the  $S$  sample,  $\mathcal{F}_i^S$  is a parameterization of the point spread function, i.e. the probability density function of reconstructing the event  $i$  at a given angular distance from the true source location,  $\mathcal{P}_{\text{sig},i}^S$  is derived from the probability density function of the energy estimator, yielding the probability of measuring the signal with the reconstructed energy of the event  $i$ ,  $\mathcal{N}^S$  is the total number of events in the  $S$  sample,  $\mathcal{B}_i^S$  is the background rate obtained from the distribution of the observed background events at the declination of event  $i$ ,  $\mathcal{P}_{\text{bkg},i}^S$  is the probability density function of the energy estimator for background and  $\mu_{\text{sig}} = \mu_{\text{sig}}^{\text{tr}} + \mu_{\text{sig}}^{\text{sh}}$  is the total number of fitted signal events.

In the likelihood maximisation, the values of  $\mu_{\text{sig}}^{\text{tr}}$  and  $\mu_{\text{sig}}^{\text{sh}}$  are left free to vary. Furthermore, the position in the sky of the fitted source is either kept fixed or allowed to be fitted within specific limits depending on the type of search (see Section 4).

In order to estimate the signal likeness of a cluster and determine the significance of any observation, a test statistic is computed as

$$Q = \log \mathcal{L}_{s+b} - \log \mathcal{L}_b, \quad (3.2)$$

where  $\log \mathcal{L}_b$  is the likelihood defined in equation (3.1) evaluated in the background-only case ( $\mu_{\text{sig}}^{\text{tr}} = \mu_{\text{sig}}^{\text{sh}} = 0$ ). The behavior of  $Q$  for different signal strengths is determined from pseudo-experiments. In each PE, a number of background events, equal to the number of selected events in data, is distributed on a sky map according to the declination-dependent distribution  $\mathcal{B}$ , together with signal events injected around a given source position.

## 4. Results

Four different searches for astrophysical neutrino sources are performed. The four approaches together with the respective results are presented below.

### 4.1 Full-Sky Search

The aim of the full-sky search is to find an excess of signal events located anywhere in the ANTARES visible sky, without making any assumption about the source position. To this purpose, the  $Q$ -value defined in equation (3.2) is evaluated in steps of  $1^\circ \times 1^\circ$  over the whole scanned region, with the location of the fitted cluster being left free to vary within these boundaries. PEs are performed to obtain the background-only  $Q$  distributions in step of  $1^\circ$  in declination. From these distributions, the probability to find a  $Q$ -value bigger than the one obtained at the cluster position, i.e. the pre-trial p-value, is calculated. The most significant cluster of this search is found at a right-ascension of  $\alpha = 343.8^\circ$  and a declination of  $\delta = 23.5^\circ$  with a pre-trial p-value of  $3.84 \times 10^{-6}$ . The post-trial significance of the cluster, obtained by comparing the pre-trial p-value to the distribution of the smallest p-values found anywhere in the sky when performing the same analysis on many PEs, is found to be 5.9% or  $1.9\sigma$  (two-sided convention). The upper limits of the highest significant



cluster in bands of  $1^\circ$  in declination at a 90% Confidence Level (C.L.) obtained using the Neyman method [7] are shown in Figure 1. The limits computed in this analysis are set on the total neutrino flux ( $\Phi_{\nu_\mu} + \Phi_{\nu_e} + \Phi_{\nu_\tau}$ ), assuming the equipartition at Earth of the three neutrino flavours.

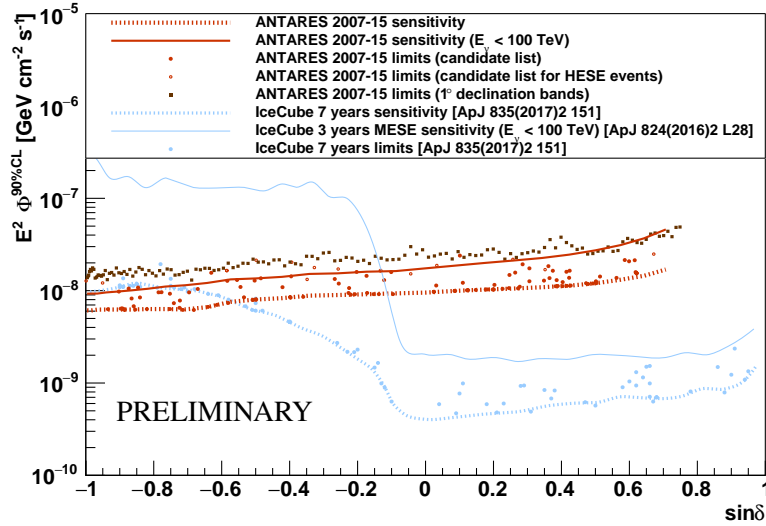


**Figure 1:** Upper limits at a 90% C.L. on the total signal flux (sum of the contributions of the three neutrinos flavours) from the investigated candidates assuming an  $E^{-2}$  spectrum (red circles). The dashed red line shows the ANTARES sensitivity and the blue dashed line the sensitivity of the seven years point-like source analysis by the IceCube Collaboration for comparison [8]. The upper-limits obtained in this analysis are also included (blue dots). The ANTARES  $5\sigma$  pre-trial discovery flux is a factor 2.5 to 2.9 larger than the sensitivity. The curve for the sensitivity for neutrino energies under 100 TeV is also included (solid red line). The IceCube curve for energies under 100 TeV (solid blue line) is obtained from the 3 years MESE analysis [9]. The limits of the most significant cluster obtained in bands of  $1^\circ$  in declination (dark red squares) are also shown.

## 4.2 Candidate List Search

In the candidate list search, the directions of a pre-selected list of 106 known astronomical objects, which are promising neutrinos emitters, are investigated to look for an excess of neutrino events. The list of the astronomical candidates along with their equatorial coordinates, fitted number of signal events and upper limits on the flux is shown in Table 1. The most signal-like cluster is found at the location of HESSJ0632+057 at  $(\alpha, \delta) = (98.24^\circ, 5.81^\circ)$ , with a pre-trial p-value of 0.16%. The post-trial significance of the cluster is 13% or  $1.5\sigma$  (two-sided convention). The sensitivities and limits calculated with the Neyman method at a 90% C.L. for this search are shown in Figure 1 as a function of the declination.

A separate candidate list search is performed to investigate the 13 IceCube (IC) HESE classified as muon tracks [10, 11, 12]. The non-negligible estimated angular error of these events is accounted for by letting the direction parameters in the likelihood maximisation free to vary around the position of the IC tracks within a cone twice as large as their estimated angular error. In Table 2 the coordinates of these events together with their angular uncertainty (provided by the IceCube



Collaboration), fitted number of signal events and upper limits on the flux derived from our analysis are shown. The HESE candidate with the largest excess in fitted signal is the IceCube track with ID 3 and  $\mu_{\text{sig}} = 5.3$ . The fitted cluster is located at  $(\alpha, \delta) = (130.1^\circ, -29.8^\circ)$ , which is at a distance of  $1.5^\circ$  from the original HESE track at  $(\alpha, \delta) = (127.9^\circ, -31.2^\circ)$ , and has an observed post-trial p-value of 0.20 ( $1.2\sigma$  significance).

### 4.3 Galactic Center Region

A restricted region defined as an ellipse around the GC with semi-axes of  $20^\circ$  in galactic longitude and  $15^\circ$  in galactic latitude is scanned to search for clustering of events with respect to the expected background as in the full-sky search (Section 4.1). The motivation of this dedicated search around the GC relies on the number of high-energy neutrino events observed by the IceCube detector [10, 11] that appear to cluster in this region. Furthermore, the HESS Collaboration recently discovered an accelerator of PeV protons in the Galactic Center [13] that could induce neutrinos. Assuming the usual  $E^{-2}$  spectrum, the most significant cluster found in this region is located at  $(\alpha, \delta) = (257.4^\circ, -41.0^\circ)$  with a pre-trial p-value of 0.09% and a post-trial significance of 60%.

Moreover, since a fit of the spectral index to the astrophysical neutrino signal detected by IceCube resulted in  $\Phi(E) \propto E^{-\gamma}$  with  $\gamma = 2.3$  [11] and  $\gamma = 2.6$  [14], slightly softer spectra than the  $E^{-2}$  dependence are tested ( $\gamma = 2.1, 2.3, 2.5$ ). Different source extensions, quantified by the  $\sigma$  of the Gaussian distribution, are also simulated ( $\sigma = 0.5^\circ, 1.0^\circ, 2.0^\circ$ ). For a spectral index of  $\gamma = 2.5$  and a point source, the most significant cluster is found at  $(\alpha, \delta) = (273.0^\circ, -42.2^\circ)$ , with a pre-trial p-value of 0.02% and a post-trial significance of 30%. The most significant clusters for the remaining spectral indices and source extensions are located within  $1^\circ$  from the latter. In Figure 2, the declination-dependent limit of this search is shown both for different energy spectral indices  $\gamma$  and different source extensions  $\sigma$ .

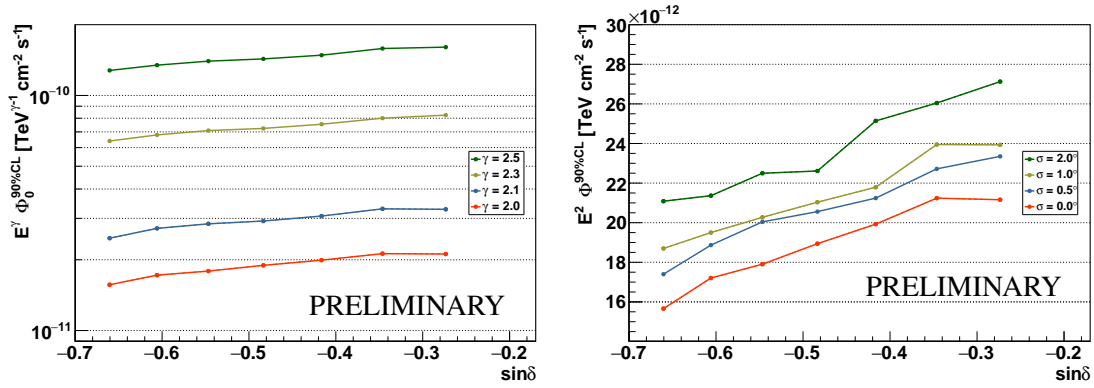


**Figure 2:** 90% C.L. upper limits of a search restricted to the region around the origin of the galactic coordinates at  $(\alpha, \delta) = (266.40^\circ, -28.94^\circ)$  assuming different spectral indices for the neutrino flux (left) and different source extensions for  $\gamma = 2$  (right).

### 4.4 Sagittarius A\*

The super-massive black hole Sagittarius A\*, located at  $(\alpha, \delta) = (266.42^\circ, -29.01^\circ)$ , is a strong candidate for cosmic neutrino production [15]. It is investigated as an extended source

Type	Name	$\delta$ [ $^{\circ}$ ]	$\alpha$ [ $^{\circ}$ ]	$\mu_{\text{sig}}$	$\Phi_0^{90\%}$	Type	Name	$\delta$ [ $^{\circ}$ ]	$\alpha$ [ $^{\circ}$ ]	$\mu_{\text{sig}}$	$\Phi_0^{90\%}$
BLLac	PKS2005-489	-48.82	302.37	0.3	0.93	Radio	PKS1406-076	-7.90	212.20	-	0.92
	PKS0537-441	-44.08	84.71	0.6	0.96		QSO2022-077	-7.60	306.40	1.0	1.64
	PKS1440-389	-39.14	220.99	2.9	1.56		3C279	-5.79	194.05	0.8	1.59
	PKS0426-380	-37.93	67.17	-	0.70		B1030+074	7.19	158.39	-	1.01
	PKS1454-354	-35.67	224.36	1.2	1.28		PKS1502+106	10.52	226.10	-	1.03
	TXS1714-336	-33.70	259.40	0.8	1.31		3C454.3	16.15	343.50	-	1.10
	PKS0548-322	-32.27	87.67	-	0.85		4C+21.35	21.38	186.23	-	1.37
	H2356-309	-30.63	359.78	-	0.79		B1422+231	22.93	216.16	-	1.12
	PKS2155-304	-30.22	329.72	-	0.80		PKS1441+25	25.03	220.99	-	1.38
	1ES1101-232	-23.49	165.91	-	0.85		PKS0625-35	-35.49	96.78	-	0.74
	1ES0347-121	-11.99	57.35	-	0.92		SNR LHA120-N-157B	-69.16	84.43	-	0.63
	RGBJ0152+017	1.79	28.17	-	1.14		RCW86	-62.48	220.68	-	0.62
	RBS0723	11.56	131.80	-	1.03		MSH15-52	-59.16	228.53	-	0.68
	PKS0235+164	16.61	39.66	2.1	1.93		SNRG327.1-01.1	-55.08	238.65	-	0.63
	RGBJ2243+203	20.35	340.98	-	1.29		RXJ0852.0-4622	-46.37	133.00	-	0.65
	VERJ0521+211	21.21	80.44	1.2	1.84		RXJ1713.7-3946	-39.75	258.25	-	0.67
	S20109+22	22.74	18.02	-	1.30		W28	-23.34	270.43	0.8	1.43
	PKS1424+240	23.79	216.75	-	1.12		SNRG015.4+00.1	-15.47	274.52	0.2	1.34
	MS1221.8+2452	24.61	186.10	-	1.13		W44	1.38	284.04	-	0.97
	1ES0647+250	25.05	102.69	-	1.65		HESSJ1912+101	10.15	288.21	-	1.03
S31227+25	25.30	187.56	-	1.14	W51C	14.19	290.75	-	1.07		
WComae	28.23	185.38	-	1.20	IC443	22.50	94.21	-	1.12		
1ES1215+303	30.10	184.45	-	1.26	Sey2 ESO139-G12	-59.94	264.41	-	0.82		
1ES1218+304	30.19	185.36	-	1.21	CentaurusA	-43.02	201.36	-	0.62		
Markarian421	38.19	166.08	-	1.59	UNID HESSJ1507-622	-62.34	226.72	-	0.62		
Binary	CirX-1	-57.17	230.17	-	0.84	HESSJ1503-582	-58.74	226.46	-	0.62	
	GX339-4	-48.79	255.70	-	0.63	HESSJ1023-575	-57.76	155.83	1.5	1.08	
	LS5039	-14.83	276.56	-	1.19	HESSJ1614-518	-51.82	243.58	0.7	0.96	
	SS433	4.98	287.96	-	0.99	HESSJ1641-463	-46.30	250.26	-	0.78	
FSRQ	HESSJ0632+057	5.81	98.24	2.7	2.40	HESSJ1741-302	-30.20	265.25	0.6	1.29	
	S30218+35	35.94	35.27	0.7	2.15	HESSJ1826-130	-13.01	276.51	-	1.07	
GC	B32247+381	38.43	342.53	-	1.54	HESSJ1813-126	-12.68	273.34	-	0.90	
	GalacticCentre	-29.01	266.42	1.1	1.36	HESSJ1828-099	-9.99	277.24	0.7	1.45	
PWN	HESSJ1356-645	-64.50	209.00	0.4	0.98	HESSJ1834-087	-8.76	278.69	-	0.92	
	HESSJ1303-631	-63.20	195.75	-	0.64	2HWCJ1309-054	-5.49	197.31	-	0.92	
	HESSJ1458-608	-60.88	224.54	1.2	1.05	2HWCJ1852+013*	1.38	283.01	-	0.97	
	HESSJ1616-508	-50.97	243.97	0.5	0.96	2HWCJ1902+048*	4.86	285.51	-	0.99	
	HESSJ1632-478	-47.82	248.04	-	0.73	MGROJ1908+06	6.27	286.99	-	1.22	
	VelaX	-45.60	128.75	-	0.62	2HWCJ1829+070	7.03	277.34	-	1.01	
	HESSJ1831-098	-9.90	277.85	-	0.95	2HWCJ1907+084*	8.50	286.79	-	1.02	
	HESSJ1837-069	-6.95	279.41	-	1.30	ICPeV	11.42	110.63	-	1.03	
	MGROJ2019+37	36.83	304.64	0.4	2.08	2HWCJ1914+117	11.72	288.68	-	1.16	
	PSRB1259-63	-63.83	195.70	-	0.64	2HWCJ1921+131	13.13	290.30	-	1.05	
Pulsar	Terzan5	-24.90	266.95	-	1.09	2HWCJ0700+143	14.32	105.12	-	1.48	
	Geminga	17.77	98.47	0.9	1.75	VERJ0648+152	15.27	102.20	-	1.57	
	Crab	22.01	83.63	0.1	1.64	2HWCJ0819+157	15.79	124.98	-	1.06	
Quasar	PKS1424-418	-42.10	216.98	1.1	1.04	2HWCJ1928+177	17.78	292.15	-	1.26	
	SwiftJ1656.3-3302	-33.04	254.07	-	1.10	2HWCJ1938+238	23.81	294.74	-	1.24	
	PKS1622-297	-29.90	246.50	-	0.80	2HWCJ1949+244	24.46	297.42	-	1.60	
	PKS0454-234	-23.43	74.27	-	0.84	2HWCJ1955+285	28.59	298.83	-	1.18	
	PKS1830-211	-21.07	278.42	-	0.86	2HWCJ1953+294	29.48	298.26	-	1.20	
	QSO1730-130	-13.10	263.30	-	0.94	2HWCJ1040+308	30.87	160.22	-	1.42	
PKS0727-11	-11.70	112.58	1.3	1.59	2HWCJ2006+341	34.18	301.55	-	1.38		

**Table 1:** List of astrophysical objects used in the candidate list search. Presented are the object's coordinates in declination ( $\delta$ ) and right-ascension ( $\alpha$ ). The first column reports the type of source: *Binary* means X-Ray binary, *GC* means Galactic Center, *Radio* means Radio Galaxy, *Sey2* means Seyfert 2 Galaxy, *UNID* means unidentified. The last two columns show the sum of the fitted number of signal track and shower events  $\mu_{\text{sig}} = \mu_{\text{sig}}^{\text{tr}} + \mu_{\text{sig}}^{\text{sh}}$ , and the 90% C.L. upper limits on the total neutrino flux normalization factor  $\Phi_0^{90\%}$  (in units of  $10^{-8} \text{ GeV cm}^{-2} \text{ s}^{-1}$ ). Candidates of the same type are sorted by declination.

HESE ID	$\delta$ [°]	$\alpha$ [°]	$\beta_{IC}$ [°]	$\mu_{sig}$	$\Phi_0^{90\%}$	HESE ID	$\delta$ [°]	$\alpha$ [°]	$\beta_{IC}$ [°]	$\mu_{sig}$	$\Phi_0^{90\%}$
3	-31.2	127.9	1.4	5.4	2.1	37	20.7	167.3	1.2	0.5	1.7
5	-0.4	110.6	1.2	0.6	1.5	38	14.0	93.3	1.2	1.0	2.1
8	-21.2	182.4	1.3	1.3	1.7	43	-22.0	206.6	1.3	0.3	1.3
13	40.3	67.9	1.2	0.8	2.4	44	0.0	336.7	1.2	1.8	1.8
18	-24.8	345.6	1.3	1.7	2.0	45	-86.3	219.0	1.2	1.6	1.2
23	-13.2	208.7	1.9	0.9	1.7	53	-37.7	239.0	1.2	3.1	1.6
28	-71.5	164.8	1.3	1.6	1.2						

**Table 2:** The 13 IceCube HESE muon track candidates [10, 12] that are in the field of view of the ANTARES detector. The table gives the equatorial coordinates, the angular error estimate  $\beta_{IC}$  of the event, the sum of the fitted number of signal track and shower events  $\mu_{sig} = \mu_{sig}^{tr} + \mu_{sig}^{sh}$  and the 90% C.L. upper limits on flux  $\Phi_0^{90\%}$  (in units of  $10^{-8} \text{ GeV cm}^{-2} \text{ s}^{-1}$ ).

with widths between  $0.5^\circ$  and  $5^\circ$ . Indeed, the high concentration of candidate sources in the GC region makes it more likely to detect an extended signal before identifying individual point-like sources. The sensitivity and upper limits obtained for the assumption of different source extensions are shown in Figure 3. The largest excess above the background is found for no extension with a pre-trial p-value of 0.22.

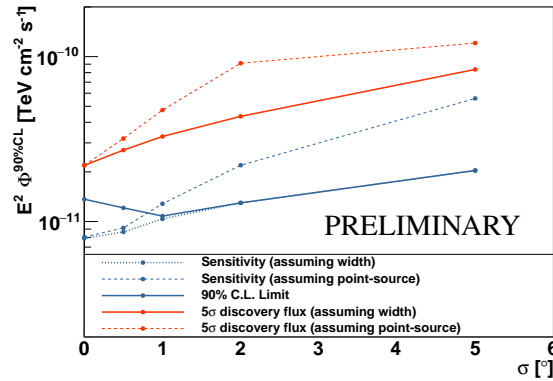


**Figure 3:** Discovery flux (solid red), median sensitivity (dotted blue) and 90% C.L. upper limits (solid blue) for a search for an extended source at Sagittarius A\* at  $(\alpha, \delta) = (266.42^\circ, -29.01^\circ)$  assuming different angular extensions  $\sigma$ . The dashed lines correspond to the point-like source assumption.

## 5. Conclusions

In this proceeding, the results of the first point-like source search that exploits the combined information from the track and shower events detected by the ANTARES telescope have been presented. Four different searches for cosmic neutrino sources have been performed: a scan over the whole ANTARES visible sky, an investigation of 106 astrophysical candidates and 13 IceCube muon tracks, a dedicated analysis of the GC region and a study of Sagittarius A\* investigated as a possible extended source. No significant evidence of cosmic neutrino sources has been found. Nevertheless, these searches provide the most sensitive limits for a large fraction of the Southern Sky, especially at neutrino energies below 100 TeV. A future joint analysis of the ANTARES events

with data from the IceCube detector could significantly improve the sensitivity of the point-like source in the Southern sky, as already shown in the past [16].

## References

- [1] M. Ageron et al. (ANTARES collaboration), *ANTARES: the first undersea neutrino telescope*, *Nucl.Instrum.Meth.* A656 (2011) 11-38 [arXiv:1104.1607]
- [2] T. Michael, *Neutrino point source search including cascade events with the ANTARES neutrino telescope*, in proceedings of *34th International Cosmic Ray Conference (ICRC 2015)*, PoS ICRC2015 (2016) 1078
- [3] A. Albert et al. (ANTARES collaboration), *First all-flavor Neutrino Point-like Source Search with the ANTARES Neutrino Telescope*, [arXiv:1706.01857]
- [4] S. Adrian-Martínez et al. (ANTARES collaboration), *Search for Cosmic Neutrino Point Sources with Four Years of Data from the ANTARES Telescope*, *Astrophys.J.* 760 (2012) 53 [arXiv:1207.3105]
- [5] F. Schüssler, *Energy reconstruction in neutrino telescopes*, in proceedings of *33rd International Cosmic Ray Conference (ICRC 2013)*
- [6] S. Adrian-Martínez et al. (ANTARES collaboration), *Measurement of the atmospheric  $\nu_\mu$  energy spectrum from 100 GeV to 200 TeV with the ANTARES telescope*, *Eur.Phys.J.* C73 (2013) 2606 [arXiv:1308.1599]
- [7] J. Neyman, *Outline of a Theory of Statistical Estimation Based on the Classical Theory of Probability*, *Phil.Trans.Roy.Soc.Lond.* A236 (1937) no.767, 333-380
- [8] M. G. Aartsen et al. (IceCube collaboration), *All-sky search for time-integrated neutrino emission from astrophysical sources with 7 years of IceCube data*, *Astrophys.J.* 835 (2017) no.2, 151 [arXiv:1609.04981]
- [9] M. G. Aartsen et al. (IceCube collaboration), *Lowering IceCube's Energy Threshold for Point Source Searches in the Southern Sky*, *Astrophys.J.* 824 (2016) no.2, L28 [arXiv:1605.00163]
- [10] M. G. Aartsen et al. (IceCube collaboration), *Observation of High-Energy Astrophysical Neutrinos in Three Years of IceCube Data*, *Phys.Rev.Lett.* 113 (2014) 101101 [arXiv:1405.5303]
- [11] M. G. Aartsen et al. (IceCube collaboration), *Searches for Extended and Point-like Neutrino Sources with Four Years of IceCube Data*, *Astrophys.J.* 796 (2014) no.2, 109 [arXiv:1406.6757]
- [12] C. Kopper et al., *Observation of Astrophysical Neutrinos in Four Years of IceCube Data*, in proceedings of *34th International Cosmic Ray Conference (ICRC 2015)*, PoS ICRC2015 (2016) 1081
- [13] A. Abramowski et al. (H.E.S.S collaboration), *Acceleration of petaelectronvolt protons in the Galactic Centre*, *Nature* 531 (2016) 476 [arXiv:1603.07730]
- [14] The IceCube Collaboration, *Observation of Astrophysical Neutrinos in Four Years of IceCube Data*, in proceedings of *34th International Cosmic Ray Conference (ICRC 2015)*, PoS ICRC2015 (2016) 1081
- [15] Y. Bai et al., *Neutrino lighthouse at Sagittarius A\**, *Phys.Rev.* D90 (2014) no.6, 063012 [arXiv:1407.2243]
- [16] S. Adrián-Martínez et al. (ANTARES and IceCube collaborations), *The First Combined Search for Neutrino Point-sources in the Southern Hemisphere With the Antares and Icecube Neutrino Telescopes*, *Astrophys.J.* 823 (2016) no.1, 65 [arXiv:1511.02149]

# Search for time correlations between ANTARES neutrino candidates and IceCube/High-Energy Starting Events

---

## J. Barrios

*IFIC - Instituto de Física Corpuscular (CSIC - Universitat de València) c/ Catedrático José Beltrán, 2 E-46980 Paterna, Valencia, Spain*

*E-mail: [javier.barrios@ific.uv.es](mailto:javier.barrios@ific.uv.es)*

## A. Coleiro

*APC, Univ Paris Diderot, CNRS/IN2P3, CEA/Irfu, Obs de Paris, Sorbonne Paris Cité, France*

*IFIC - Instituto de Física Corpuscular (CSIC - Universitat de València) c/ Catedrático José Beltrán, 2 E-46980 Paterna, Valencia, Spain*

*E-mail: [alexis.coleiro@ific.uv.es](mailto:alexis.coleiro@ific.uv.es)*

## G. Illuminati\*

*IFIC - Instituto de Física Corpuscular (CSIC - Universitat de València) c/ Catedrático José Beltrán, 2 E-46980 Paterna, Valencia, Spain*

*E-mail: [giulia.illuminati@ific.uv.es](mailto:giulia.illuminati@ific.uv.es)*

## on behalf of the ANTARES Collaboration

We present a search for ANTARES neutrino events in spatial and temporal coincidence with IceCube High-Energy Starting Events (HESE). This analysis uses a maximum likelihood ratio approach based on track events due to muons induced by neutrino interactions observed with ANTARES. Each HESE is treated as the signature of a potential transient neutrino source while the neutrino burst duration, the source direction and the number of ANTARES signal events are obtained as those maximising the likelihood. Before applying the method to the unblinded ANTARES dataset, its sensitivity and discovery potential are computed through dedicated pseudo-experiments. This study provides an effective way to acquire information on the possible origin of the IceCube astrophysical signal from transient sources.

*35th International Cosmic Ray Conference – ICRC217-  
10-20 July, 2017  
Bexco, Busan, Korea*

---

\*Speaker.

## 1. Introduction

High-energy neutrinos are expected to be produced in cosmic-ray sources. Since they are electrically neutral, weakly interacting and traveling straight from their source without suffering from absorption, neutrinos are unique messengers to further understand the particle acceleration processes in such astrophysical sources.

A high-energy neutrino diffuse flux of cosmic origin has been identified by the IceCube telescope (see e.g. [1]), the sources of which have not been identified yet. In this context, it was pointed out that two of the so-called IceCube High-Energy Starting Events (HESE) occurred within 1 day of each other with a p-value of 1.6% [2]. Consequently, this was interpreted as the signature of a possible transient point source of very high-energy neutrinos in this part of the sky.

When dealing with transient emissions, the background of atmospheric neutrinos can be significantly reduced using a time-dependent approach that consists in searching for astrophysical neutrinos in smaller time windows around source flares (see e.g. [3]).

Here, we propose a model-independent approach based on the timing properties of both the ANTARES and IceCube data samples. In particular, we search for correlations in space and time between ANTARES muon neutrino candidates and thirteen muon track HESE previously published by the IceCube collaboration. The analysis uses a maximum likelihood ratio approach where each HESE is treated as the signature of a potential transient neutrino source while the neutrino burst duration, the number of ANTARES signal events and the source position are obtained as those maximising the likelihood.

Section 2 reports the IceCube and ANTARES datasets used in this analysis. The method used in the analysis is presented in section 3, while section 4 provides with the preliminary sensitivity and discovery potential, before concluding in section 5.

## 2. Data Sample

This analysis makes use of the thirteen HESE muon track candidates<sup>1</sup> detected by the IceCube neutrino telescope within the field-of-view of the ANTARES detector. They have been observed from September 2010 to April 2014 with a median angular error of  $\sim 1.3^\circ$  (see table 1).

Data of the ANTARES neutrino telescope [5] collected from March 01, 2010 to October 31, 2014 are used in order to overlap the IceCube dataset and to search for flares lasting up to 6 months. Only events reconstructed as muon tracks are included in the dataset. These events are reconstructed by means of a multi-step procedure that estimates the direction and position of the muon using a maximum likelihood fit [6]. Events are selected applying cuts on parameters provided by the reconstruction mechanism: the reconstructed zenith angle ( $\cos \theta > -0.1$ ), the estimated angular error ( $\beta < 1^\circ$ ) and the parameter that describes the quality of the reconstruction ( $\Lambda > -5.2$ ). Further cuts are applied on energy-related variables to guarantee the validity of the muon energy estimator employed in this analysis – an approximation of the muon energy deposit per unit path

<sup>1</sup>HESE shower candidates observed by IceCube are not taken into account yet due to their larger angular error which requires more computing time for time-dependent analyses.

HESE ID	$\delta$ [°]	$\alpha$ [°]	$\beta_{IC}$ [°]	Observation Time (MJD)
3	-31.2	127.9	1.4	55451.0707482
5	-0.4	110.6	1.2	55512.5516311
8	-21.2	182.4	1.3	55608.8201315
13	40.3	67.9	1.2	55756.1129844
18	-24.8	345.6	1.3	55923.5318204
23	-13.2	208.7	1.9	55949.5693228
28	-71.5	164.8	1.3	56048.5704209
37	20.7	167.3	1.2	56390.1887627
38	14.0	93.3	1.2	56470.11038
43	-22.0	206.6	1.3	56628.56885
44	0.0	-23.3	1.2	56671.87788
45	-86.3	219.0	1.2	56679.20447
53	-37.7	239.0	1.2	56767.06630

**Table 1:** The 13 IceCube HESE muon track candidates [1, 4] that are in the field of view of the ANTARES detector. The table gives the equatorial coordinates, the angular error estimate  $\beta_{IC}$  and the date of observation of the event.

length, hereafter referred as  $\rho$  [7, 8]. These cuts were optimized for the latest ANTARES point-source analysis as detailed in [9]. The distribution of  $\Lambda$  and  $\beta$  for data, simulated cosmic and atmospheric neutrinos and atmospheric muons is shown in Figure 1. The selection yields a total of 4391 neutrino candidates.

### 3. Search Method

An unbinned method based on an extended maximum likelihood ratio test statistic is employed to look for clusters of events in time and spatial coincidence with the HESE candidates. The used likelihood is defined as

$$\log \mathcal{L}_{s+b} = \sum_i \log \left[ \mu_{\text{sig}} \mathcal{S}_i + \mathcal{N} \mathcal{B}_i \right] - \mu_{\text{sig}}, \quad (3.1)$$

where  $\mathcal{S}_i$  and  $\mathcal{B}_i$  are the values of the signal and background probability density functions (PDFs) for the event  $i$ ,  $\mu_{\text{sig}}$  is the number of fitted signal events and  $\mathcal{N}$  is the total number of events in the data sample. To improve the signal-to-background discrimination, the combined information of three parameters – direction, energy and observation time – is included in the definition of the signal and background PDFs. For each event  $i$ , the probability of being reconstructed as signal or background is given by

$$\mathcal{S}_i = \mathcal{S}^{\text{space}}(\Delta\Psi_i, \beta_i) \cdot \mathcal{S}^{\text{energy}}(\rho_i, \beta_i | \delta_i) \cdot \mathcal{S}^{\text{time}}(t_i), \quad (3.2)$$

$$\mathcal{B}_i = \mathcal{B}^{\text{space}}(\delta_i) \cdot \mathcal{B}^{\text{energy}}(\rho_i, \beta_i | \delta_i) \cdot \mathcal{B}^{\text{time}}(t_i). \quad (3.3)$$



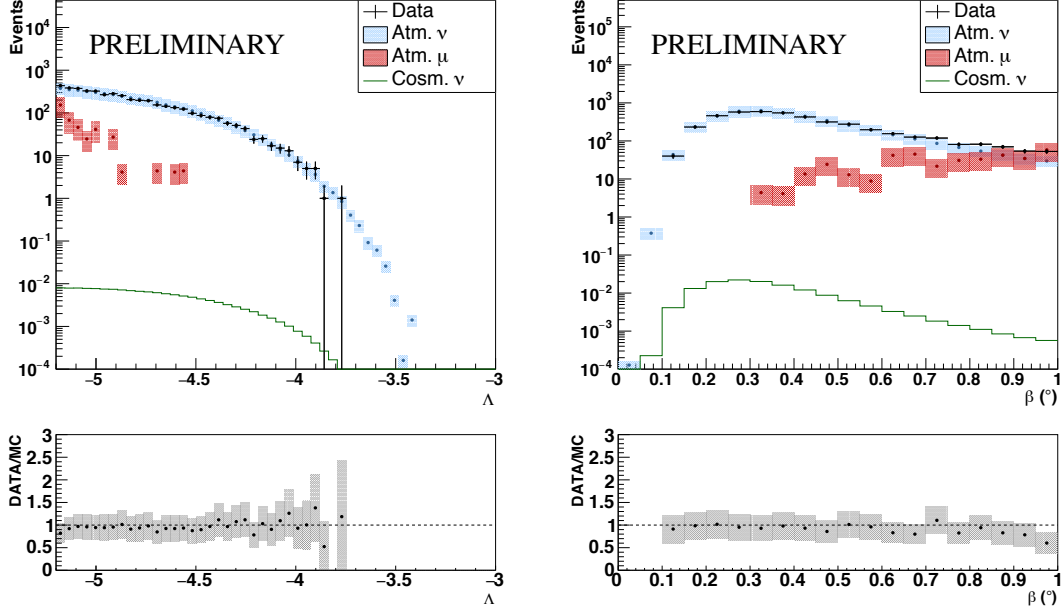


**Figure 1:** Comparison between data and Monte-Carlo simulation of atmospheric muons, atmospheric neutrinos and expected cosmic signal (assuming a spectrum  $dN/dE = 10^{-8}(E/\text{GeV})^{-2.5} \text{ GeV}^{-1} \text{ cm}^{-2} \text{ s}^{-1}$ ). Distribution of the  $\Lambda$  and  $\beta$  quality parameters are shown respectively on the left and right. The two bottom plots show the ratio data to Monte-Carlo, where the number of Monte-Carlo events is the sum of atmospheric muons and neutrinos. This figure corresponds to the event distribution after all selection criteria.

respectively. A description of each component is given below.

$\mathcal{S}^{space}(\Delta\Psi_i, \beta_i)$  is a parameterization of the point spread function, i.e. the probability density function of reconstructing the event  $i$  at a given angular distance  $\Delta\Psi_i$  from the true source location. The information of the event angular error estimate  $\beta_i$  is also included. The shape of this PDF is determined from Monte-Carlo simulations of cosmic neutrinos assuming an  $E^{-2.5}$  energy spectrum.

$\mathcal{S}^{energy}(\rho_i, \beta_i | \delta_i)$  and  $\mathcal{B}^{energy}(\rho_i, \beta_i | \delta_i)$  give the probability for a signal or background event to be reconstructed with an energy estimator  $\rho_i$  and an angular error estimate  $\beta_i$ . The dependence of the energy estimator on the declination  $\delta_i$  of the event is taken into account by generating both the PDFs in steps of 0.2 over  $\sin \delta$ . Monte-Carlo simulations of  $E^{-2.5}$  energy spectrum cosmic neutrinos (signal) and of atmospheric neutrinos (background) are used to derive the energy PDFs.

$\mathcal{S}^{time}(t_i)$  is the signal time-dependent PDF, defined as a Gaussian function:  $\mathcal{S}^{time}(t_i) = \frac{1}{\sqrt{2\pi}\sigma_i} e^{-\frac{(t_i - t_{HESE})^2}{2\sigma_i^2}}$ . Here,  $t_i$  is the arrival time of the event  $i$ ,  $t_{HESE}$  is the observation time of the HESE candidate, and  $\sigma_i$  is the fitted flare duration.

$\mathcal{B}^{space}(\delta_i)$  yields the probability of reconstructing a background event with a certain declination  $\delta_i$ . It is derived from data using the observed declination distribution of the selected events.

$\mathcal{B}^{time}(t_i)$  describes the probability to have a background event at a given time  $t_i$ . This PDF is built using the time distribution of both up-going and down-going data events required to satisfy looser selection criteria ( $\Lambda > -5.4$  and  $\beta < 1^\circ$ ). This reduces statistical fluctuations while ensuring a good reconstruction quality.

The number of signal events  $\mu_{sig}$  and the flare duration  $\sigma_t$  are fitted in the likelihood maximization. Moreover, the position in the sky of the fitted source is left free to vary around the position of the IC track within a cone twice as large as the estimated angular error.

The performances of the presented time-dependent analysis are determined by means of pseudo-experiments (PEs), i.e. performing the search for time and spatial correlation on blinded data. In each PE, a fake sky-map containing a number of background events equal to the amount of selected data events and a number of signal events ranging between 0 and 30, is generated. The simulated directions of the background events are randomly drawn from the zenith and azimuth distributions of the selected data. The distribution of the reconstructed zenith angle is shown in Figure 2. Using a time randomly extracted from the time distribution of the data events selected with a looser set of cuts, the equatorial coordinates are computed.

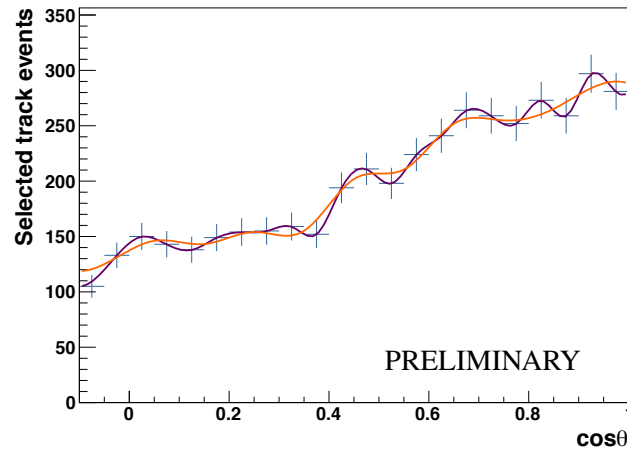


**Figure 2:** Number of selected data events as a function of the reconstructed zenith angle. The distribution of the background rate is parametrised by two different spline functions,  $P(\theta)$  and  $O(\theta)$  (the purple and orange lines). In order to account for possible systematic uncertainties on the background, the zenith-dependent distribution of background events,  $\mathcal{B}(\theta)$ , in each PE is determined as  $\mathcal{B}(\theta) = O(\theta) + r \cdot (P(\theta) - O(\theta))$ , with  $r$  being a random number drawn from a uniform distribution between -1 and 1.

The simulated signal events are injected around a given source position (one of the 13 HESE candidates) and are assigned a time drawn from a Gaussian function characterized by a mean and a sigma given by the HESE observation time and the tested flare duration respectively. In each PE, the position of the 13 HESE candidates is scanned to look for clustering of events with respect to the expected background. The signal likeness of a cluster is determined by a test statistic computed as

$$Q = \log \mathcal{L}_{s+b} - \log \mathcal{L}_b, \quad (3.4)$$

where  $\log \mathcal{L}_b$  is the likelihood defined in equation (3.1) evaluated in the background-only case ( $\mu_{\text{sig}} = 0$ ). Figure 3 shows an example of fake sky-map with the simulated background events and the positions of the 13 HESE.

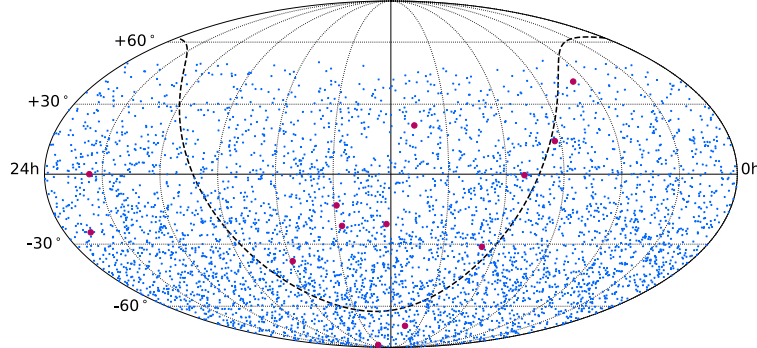


**Figure 3:** Sky-map of the scrambled background events (blue dots). The position of the 13 HESE tracks is also shown (magenta dots).

#### 4. Estimated performances

The detection power (at 50% confidence level) and sensitivity of the analysis are estimated through pseudo-experiments performed as described above.

Figure 4 shows the preliminary discovery potential and sensitivity for the IceCube HESE with ID 3 as a function of the flare duration.

The ANTARES data are currently blinded. They will be unblinded after having added ANTARES shower events. The 29 high-energy muon events observed by IceCube [10] will be added to the dataset as well before unblinding the analysis.

#### 5. Conclusions

A time-correlation analysis between the IceCube/HESE muon track sample and ANTARES muon neutrino candidates observed from 2010 to 2014 has been presented. Using a maximum likelihood ratio approach, it provides with a new way to constrain the origin of the IceCube astrophysical signal from possible transient sources. Limits can be set on the maximal amount of signal events in ANTARES related to a flare of a certain duration. Preliminary results show that sensitivity and discovery potential are better by at least a factor of two compared to time-integrated analyses. In the near future, ANTARES shower events will be included in the analysis and the 29 high-energy muon events observed by IceCube [10] will be added to the dataset as well. The analysis will be unblinded afterwards.

#### References

- [1] M. G. Aartsen et al. (IceCube collaboration), *Observation of High-Energy Astrophysical Neutrinos in Three Years of IceCube Data*, *Phys.Rev.Lett.* 113 (2014) 101101 [arXiv:1405.5303]

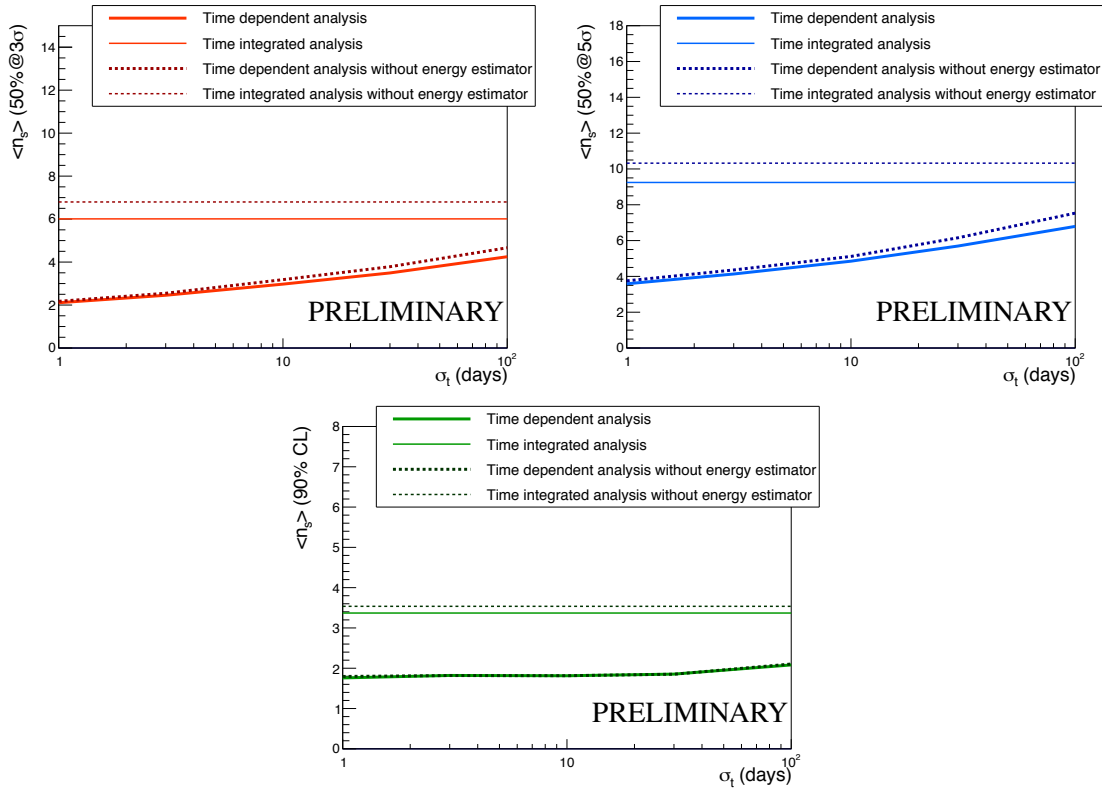


**Figure 4: Upper panel:** Post-trial  $3\sigma$  and  $5\sigma$  discovery potential (left and right plots respectively) expressed as the mean number of detected events  $\langle n_s \rangle$  for IceCube HESE #3 as a function of the flare duration for the time dependent analysis (solid thick line) and for the time integrated analysis (solid thin line). The curves for the case in which the energy information is not used in the likelihood are also shown. **Lower panel:** Pre-trial sensitivity expressed as the mean number of detected events  $\langle n_s \rangle$  for IceCube HESE #3 as a function of the flare duration for the time dependent analysis (solid thick line) and for the time integrated analysis (solid thin line). The curves for the case in which the energy information is not used in the likelihood are also shown.

- [2] Y. Bai et al., *Neutrino lighthouse at Sagittarius A\** *Phys. Rev. D* 90 (2014) 063012 [arXiv:1407.2243]
- [3] A. Albert et al. (ANTARES collaboration), *Time-dependent search for neutrino emission from X-ray binaries with the ANTARES telescope* *JCAP* 4 (2017) 019 [arXiv:1609.07372]
- [4] C. Kopper et al., *Observation of Astrophysical Neutrinos in Four Years of IceCube Data*, in proceedings of *34th International Cosmic Ray Conference (ICRC 2015)*, [PoS ICRC2015 \(2016\) 1081](#)
- [5] M. Ageron et al. (ANTARES collaboration), *ANTARES: the first undersea neutrino telescope*, *Nucl.Instrum.Meth.* A656 (2011) 11-38 [arXiv:1104.1607]
- [6] S. Adrian-Martínez et al. (ANTARES collaboration), *Search for Cosmic Neutrino Point Sources with Four Years of Data from the ANTARES Telescope*, *Astrophys.J.* 760 (2012) 53 [arXiv:1207.3105]
- [7] F. Schüssler, *Energy reconstruction in neutrino telescopes*, in proceedings of *33rd International Cosmic Ray Conference (ICRC 2013)*

- [8] S. Adrian-Martínez et al. (ANTARES collaboration), *Measurement of the atmospheric  $\nu_\mu$  energy spectrum from 100 GeV to 200 TeV with the ANTARES telescope*, *Eur.Phys.J. C* 73 (2013) 2606 [arXiv:1308.1599]
- [9] A. Albert et al. (ANTARES collaboration), *First all-flavor Neutrino Point-like Source Search with the ANTARES Neutrino Telescope*, [arXiv:1706.01857]
- [10] M.G.Aartsen et al. (IceCube collaboration), *Observation and Characterization of a Cosmic Muon Neutrino Flux from the Northern Hemisphere using six years of IceCube data*, *Astrophys. J.* 833 (2016) 3 [arXiv:1706.01857]